TECHNISCHE UNIVERSITÄT WIEN

DIPLOMARBEIT

Dichotomy Between Local and Uniform Compressibility in Correlated Systems: The Role of the Irreducible Vertex

zur Erlangung des akademischen Grades

Diplom-Ingenieur

im Rahmen des Studiums

Technische Physik

eingereicht von

Matthias Reitner, BSc
Matrikelnummer 01325200

ausgeführt am Institut für Festkörperphysik
der Fakultät für Physik der Technischen Universität Wien

Betreuung
Betreuer: Associate Prof. Dr. Alessandro Toschi
Mitwirkung: Projektass.(FWF) Dipl.-Ing. Patrick Chalupa, BSc

Wien, 29.3.2020

Matthias Reitner	Alessandro Toschi

Abstract

Vertex divergences, observed ubiquitously in all fundamental many-electron models, have important and known consequences on a theoretical and algorithmic level. On the one hand they are connected to the multivaluedness of the Luttinger-Ward functional, on the other hand they hamper the use of cutting-edge algorithms, which extend dynamical mean-field theory (DMFT) solutions to the non-local case. It is understood that vertex divergences are generally originated by the suppression of local fluctuations. While the origin is quite clear, the question of their physical implications is still left open.

In this work we unveil a novel physical effect of these divergences for the one-band Hubbard model on the square-lattice, solved with DMFT. By decomposing the local and uniform susceptibilities in terms of their spectral representation, we show that certain vertex divergences can be associated to a sign-flip of the effective electronic interaction from attractive to repulsive. This is ultimately responsible for the enhancement and even the divergence of the charge compressibility in proximity to the critical endpoint of the Mott metal-insulator transition in the Hubbard model. Thereby, we gain a deeper understanding of the phase-transitions in the non-perturbative regime of strongly correlated electron systems. These findings are of possible relevance for the physics of the Hund's metals and also explain why no pairing- or charge-density-wave-instabilities can be triggered by this mechanism in single orbital systems.

Kurzfassung

Vertexdivergenzen, werden allgegenwärtig in allen fundamentalen Vielelektronenmodellen beobachtet und haben wichtige und bekannte Auswirkungen auf theoretischer und algorithmischer Ebene. Einerseits stehen sie mit der Mehrdeutigkeit des Luttinger-Ward-Funktionals in Verbindung, andererseits hindern sie die Verwendung von modernsten Algorithmen, die Lösungen der dynamischen Molekularfeldtheorie (DMFT) auf den nichtlokalen Fall hin erweitern. Es gilt als verstanden, dass Vertexdivergenzen generell durch die Unterdrückung lokaler Fluktuationen entstehen, dabei bleibt die Frage ihrer physikalischen Implikationen jedoch unbeantwortet.

In dieser Arbeit enthüllen wir einen neuartigen physikalischen Effekt dieser Divergenzen für das mit DMFT berechnete Einband-Hubbard-Modell am quadratischen Gitter. Dabei zeigen wir, dass bestimmte Vertexdivergenzen mit dem Vorzeichenwechsel der effektiven Elektron-Wechselwirkung zusammenhängen, indem wir die lokale und uniforme Ladungssuszeptibilität in ihre spektrale Darstellung zerlegen. Letztendlich führt dies zur Erhöhung und sogar zur Divergenz der Kompressibilität in der unmittelbaren Nähe des kritischen Punktes des Mott-Metall-Isolator-Übergangs im Hubbard-Modell. Dadurch erreichen wir ein tieferes Verständnis für Phasenübergänge im nicht-störungstheoretischen Bereich stark korrelierter Elektronenysteme. Diese Resultate sind einerseits von möglicher Relevanz für die Physik von Hundschen Metallen und erklären andererseits, warum dieser Mechanismus keine Pairing- oder Charge-Density-Wave-Instabilitäten auslösen kann.

Acknowledgements

There is no doubt that this thesis would not have been possible without the great support from so many people, who I want to express my deepest gratitude.

First, I want to sincerely thank my two supervisors, Alessandro Toschi and Patrick Chalupa, who gave me the opportunity to work on such an interesting topic and inspired me with their everlasting interest in physics and vertex functions. Their tireless support and dedication were always overwhelming and made me a truly fortunate master student. I also want to thank Alessandro for always having the time to give me a deeper and clear insight on the physical problems I faced, and for teaching me so much about the physics of strong correlations. In addition, he gave me the opportunity to already publish my first paper and to apply for and attend the autumn school on correlated electrons in Jülich. Furthermore, I am indebted to Patrick for helping me at every opportunity e.g. by patiently teaching me the use of *w2dynamics* and for assisting me with the many problems of the computations. Also thank you both, for the multiple invitations on espressi.

I would also like to thank Thomas Schäfer, who was involved in the programming of the DΓA post-processing script, and Alexander Vock who performed similar calculations for their help in setting up the tools for the two-particle analysis. I want to thank Lorenzo Del Re, Daniel Springer, Sergio Ciuchi, Thomas Schäfer, Gerorg Rohringer for the insightful discussions as well as Giorgio Sangiovanni for the opportunity to present and discuss my results at the university in Würzburg.

Additionally, I also would like to thank Paul Worm for our countless discussions about various topics in our office, providing me a motivating and unique work experience (by the way, Python is the truly better language). Furthermore, I would like to thank the other master and PhD students e.g. Matthias Pickem, Severino Adler, Benjamin Klebel, to name just a few, for the special atmosphere at the university.

To my family, my grandparents, my parents Heinz and Elisabeth as well was my brother Jakob, I want to express my deepest gratitude for always supporting me throughout the years and enabling me the opportunity to pursue my interests and develop my curious mind, which lead me on this path.

And Kati, thank you for everything.

Contents

Chapter 1

Introduction

The theoretical description of the many body problem in condensed matter remains a major challenge in today's solid-state physics. Although for a wide range of materials density functional theory (DFT) [1] provides a satisfactory description, by considering independent (auxiliary) particles in a static mean-field, for materials which exhibit strongly correlated electrons – such as transition metal oxides and rare earth compounds, with localised d and f orbitals – DFT fails in correctly describing the physics. This breakdown of the theory reflects the failure of capturing strong electronic correlations beyond the independent particle picture. Generally, in these classes of compounds, correlation effects are so large to render a quantum many-body perturbation similar to that of QED not formally justified. At the same time, these materials show a rich variety of interesting phenomena, e.g. Mott metal-insulator transitions, high-temperature superconductivity, quantum criticality, heavy fermion behaviour and many more [2].

A major theoretical progress achieved in the last three decades was the development of the dynamical mean field theory (DMFT) [3, 4]. This quantum extension of the classical mean field concept, which is exact in the limit of infinite dimensions, allows to go beyond the perturbative regime and enables to correctly describe the Mott insulating phase, though still neglecting non-local correlations. These non-local correlations are, however, of great importance for the high-temperature superconductivity. One way to include these effects, and to go beyond the limitations of DMFT, is to use its diagrammatic extensions [5, 6]. These approaches build upon the idea of extracting two-particle (2P) correlation functions from the DMFT solution. These are then exploited as a starting point to construct Feynman diagrammatic theories, which include non-local correlations on top of the non-perturbative physics captured by DMFT. However, in the strongly correlated regime, unexpected divergences in the 2P-irreducible vertex functions, a key ingredient for some diagrammatic extension schemes, were discovered [7–11]. Evidently, these divergences represent a problem for these cutting-edge non-perturbative algorithms. They are also connected to the multivaluedness of the generating functional of the vertex functions, i.e. the Luttinger-Ward functional [12].

These vertex divergences appear to be not a mere a mathematical peculiarity, having a physical connection to the suppression of the local charge fluctuations driven by the strong electronic repulsion [13]. The aim of this work is to investigate this connection further, by studying the enhancement of the compressibility, and thus the underlying generalized charge susceptibility (see Fig. 1.1), observed near the Mott transition in the hole doped Hubbard model [14, 15]. Thereby, we hope to identify an additional, and possibly stronger, connection between the above-mentioned vertex divergences and true thermodynamic transitions.

This thesis is organised in the following way: in chapter 2 we give a concise introduction into the theoretical formalism necessary for the understanding of the following chapters and present our model and method, in chapter 3 we set the stage for the physical interpretation of our work. In chapter 4 our results are shown. Concluding remarks and a possible outlook can be found in the last chapter 5.

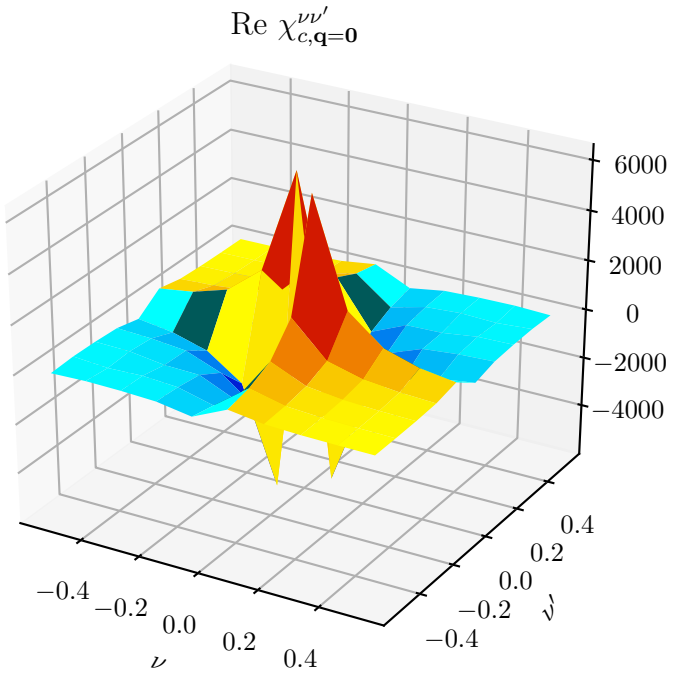

FIG. 1.1: Real part of the uniform generalised charge susceptibility $\chi^{\nu\nu'}_{c,\mathbf{q}=\mathbf{0}}$ in the Hubbard-model on a square-lattice at $U = 2.4,\ T = 1/53,\ \mu = 1.1$. To be discussed in chapter 4.

Chapter 2

General Formalism

"E sempre questa storia!"
-Umberto Tozzi

In this chapter, the necessary theoretical framework for this thesis is introduced. Starting with an overview of the Green's function formalism for one and two-particle interactions in the first section, we proceed with a description of the electronic model used in our study, i.e. the Hubbard model. In the third section the key method for studying strong correlations in this model is presented, namely the Dynamical Mean Field Theory (DMFT). The Mott Insulator Transition (MIT) in the single orbital Hubbard Model is discussed in section four. In the last section of this chapter, we briefly illustrate the Continuous Time Quantum Monte Carlo in the Hybridization Expansion (CT-HYB) as our method of choice for the DMFT calculations.

2.1 Green's Functions

In solid state physics – where one is often dealing with huge numbers of particles of order of 10^{23} – a microscopic description of single electrons and atoms is in general not feasible, the computational effort for a direct treatment of such large numbers of interacting particles exceeds even the capacity of modern supercomputers. But even if the calculations were possible, an exact microscopic description might not even be of great utility. In fact, one is rather eager to study the macroscopic or collective properties of the whole system than the behaviour of single electrons individually. After all, the excitations and responses of the solid – resulting from external perturbations and forces on the material, e.g. electromagnetic fields, temperature gradients etc. – reflect its physical properties and behaviour and correspond to the practical situation occurring in a lab and even in the all-day life. Although in the general case, mutual interactions between nuclei and electrons drive important and interesting phenomena. The time scales of their dynamics are very different. Hence it is often possible to decouple their degrees of freedom and focus on the electrons in an effective lattice potential of the nuclei, e.g. in approximative models like the Hubbard model in this thesis.

A natural framework to study such many electron problems is provided by the Green's functions formalism in second quantisation, which we will briefly introduce in the following. For a more general introduction into the Green's functions formalism and the fundamentals of quantum many body physics we refer the reader to Refs. [16–18]. A more comprehensive discussion focussing on the two particle formalism discussed in Sec. 2.1.3, can be found in Refs. [6, 19, 20].

2.1.1 Matsubara Formalism

For an intuitive understanding of the Green's function formalism let us introduce the one-particle (time-ordered) Green's function, which is defined ($\hbar = 1$) as

$$G^{(1)}_{C,\sigma_1\sigma_2}(\mathbf{r}_1, t_1, \mathbf{r}_1, t_2) \coloneqq -\mathrm{i}\left\langle \mathbf{T}\hat{c}^\dagger_{\sigma_1}(\mathbf{r}_1, t_1)\hat{c}_{\sigma_2}(\mathbf{r}_2, t_2)\right\rangle . \tag{2.1}$$

Here, $\hat{c}^\dagger_{\sigma_1}(\mathbf{r}_1, t_1) = \mathrm{e}^{\mathrm{i}\hat{\mathcal{H}}t_1}\hat{c}^\dagger_{\sigma_1}(\mathbf{r}_1)\mathrm{e}^{-\mathrm{i}\hat{\mathcal{H}}t_1}$ denotes a creation operator of a particle at time and position $t_1, \mathbf{r}_1$ and $\hat{c}_{\sigma_2}(\mathbf{r}_2, t_2) = \mathrm{e}^{\mathrm{i}\hat{\mathcal{H}}t_2}\hat{c}_{\sigma_2}(\mathbf{r}_2)\mathrm{e}^{-\mathrm{i}\hat{\mathcal{H}}t_2}$ a corresponding annihilation operator at $t_2, \mathbf{r}_2$. $\hat{\mathcal{H}}$ is the Hamiltonian of the system and $\langle ... \rangle$ denotes the expectation value at finite temperature $T = 1/\beta$, which is performed as

$$\langle ... \rangle = \frac{1}{Z}\,\mathrm{Tr}\left(\mathrm{e}^{-\beta\hat{\mathcal{H}}}...\right) \quad \text{with} \quad Z = \mathrm{Tr}\left(\mathrm{e}^{-\beta\hat{\mathcal{H}}}\right), \tag{2.2}$$

by calculating the trace Tr over a complete set of states. For a system where the number of particles is not fixed, we replace $\hat{\mathcal{H}}$ in Eq. (2.2) by $(\hat{\mathcal{H}} - \mu\hat{\mathcal{N}})$, where μ is the chemical potential and $\hat{\mathcal{N}}$ the particle number operator. $\mathbf{T}$ in Eq. (2.1) represents the time-ordering operator which permutes the operators after its time argument in descending order, by putting operators at later times to left. Each permutation of two fermionic operators gives an additional minus sign in Eq. (2.1).

Thus, for $t_2 > t_1$ one can understand the one-particle (time-ordered) Green's function as the expectation value of a particle which is added to the system at time t_1, is propagated till t_2, and will be then removed. Whereas for $t_1 > t_2$ the particle will be removed first and then the remaining *hole* is propagated until the particle is finally added to the system again.

In most cases the Hamiltonian can be written as $\hat{\mathcal{H}} = \hat{\mathcal{H}}_0 + \hat{\mathcal{V}}$, where only $\hat{\mathcal{H}}_0$ can be solved exactly and $\hat{\mathcal{V}}$ contains a perturbation to the system. However $\hat{\mathcal{V}}$ appears in Eq. (2.1) at two different places. Once in the thermal expectation value in the factor $\mathrm{e}^{-\beta\hat{\mathcal{H}}}$ and also in the time propagation $\mathrm{e}^{\pm\mathrm{i}\hat{\mathcal{H}}t}$. Performing a perturbation expansion in both factors is clearly very cumbersome, therefore it is often more convenient to use the Matsubara formalism by performing a Wick rotation and switching to imaginary times $\tau = \mathrm{i}t$. In this way both factors can be treated as depending on real parameters defined on the same axis.

Omitting spatial arguments $\mathbf{r}_i$, we thus define the (n)-particle Green's function in the Matsubara formalism now as

$$G^{(n)}_{\sigma_1\sigma_2...\sigma_{2n}}(\tau_1, \tau_2, ..., \tau_{2n}) \coloneqq \left\langle \mathcal{T}\hat{c}^\dagger_{\sigma_1}(\tau_1)\hat{c}_{\sigma_2}(\tau_2)...\hat{c}_{\sigma_{2n}}(\tau_{2n})\right\rangle . \tag{2.3}$$

$\hat{c}^{(\dagger)}_{\sigma_i}(\tau_i) = \mathrm{e}^{\hat{\mathcal{H}}\tau_i}\hat{c}^{(\dagger)}_{\sigma_i}\mathrm{e}^{-\hat{\mathcal{H}}\tau_i}$ is now the (creation)/annihilation operator in imaginary times and $\mathcal{T}$ the imaginary time-ordering operator.

To ensure that the expression in Eq. (2.3) remains finite, all time arguments τ_i must be located within an interval $\Delta\tau$ of length β. Otherwise the term $\mathrm{e}^{-(\beta-\Delta\tau)\hat{\mathcal{H}}}$ in the definition of the (n)-particle Green's function would lead to exponential increasing contributions. By using the cyclic property of the trace, one can then show that the (n)-particle Green's function in the Matsubara formalism is periodic/antiperiodic in regard to the transformation $\tau_i \to \tau_i + \beta$ when $\hat{c}^{(\dagger)}_{\sigma_i}(\tau_i)$ are bosonic/fermionic operators. Therefore we can restrict every imaginary time argument τ_i to the range [19, 20]

$$0 \leq \tau_i \leq \beta. \tag{2.4}$$

This periodic/antiperiodic property of the (n)-particle Green's function on the finite interval $[0, \beta]$ has important consequences for the Fourier expansion:

$$\begin{aligned} G^{(n)}_{\sigma_1 \ldots \sigma_{2n}}(\tau_1, ..., \tau_{2n}) &= \frac{1}{\beta^{2n}} \sum_{\nu_1, ..., \nu_{2n}} \mathrm{e}^{\mathrm{i}(\nu_1\tau_1 + ... - \nu_{2n}\tau_{2n})} G^{(n)}_{\sigma_1 \ldots \sigma_{2n}}(\nu_1, ..., \nu_{2n}), \\ G^{(n)}_{\sigma_1 \ldots \sigma_{2n}}(\nu_1, ..., \nu_{2n}) &= \int_0^\beta \mathrm{d}\tau_1 \ ... \int_0^\beta \mathrm{d}\tau_{2n} \ e^{-\mathrm{i}(\nu_1\tau_1 + ... - \nu_{2n}\tau_{2n})} G^{(n)}_{\sigma_1 \ldots \sigma_{2n}}(\tau_1, ..., \tau_{2n}), \end{aligned} \tag{2.5}$$

where we adopted the rather unfortunate notation of $G^{(n)}_{\sigma_1 \ldots \sigma_{2n}}(\nu_1, ..., \nu_{2n})$ being the Fourier transform of $G^{(n)}_{\sigma_1 \ldots \sigma_{2n}}(\tau_1, ..., \tau_{2n})$. The $\nu_i = \frac{\pi}{\beta}(2n_i)/\nu_i = \frac{\pi}{\beta}(2n_i + 1)$ are now discrete bosonic/fermionic Matsubara frequencies, with $n_i \in \mathbb{Z}$. For better clarity, we will further use ω_i and ν_i for the notation of bosonic and fermionic Matsubara frequencies respectively.

If we want to extend Eq. (2.5) again for Green's functions depending on $\mathbf{r}_i$, e.g on lattice sites $\mathbf{R}_i$, we can replace every imaginary time argument τ_i by the four-vector $(\tau_i, \mathbf{R}_i)$ and the Matsubara frequencies likewise with $(\nu_i, \mathbf{k}_i)$. Of course, we then also have to replace

$$\frac{1}{\beta} \sum_{\nu_i} \mathrm{e}^{\mathrm{i}\nu_i\tau_i} \to \frac{1}{\beta} \sum_{\nu_i} \sum_{\mathbf{k}_i} \mathrm{e}^{\mathrm{i}(\nu_i\tau_i - \mathbf{k}_i\mathbf{R}_i)} \quad \text{and} \quad \int_0^\beta \mathrm{d}\tau_i \to \sum_{\mathbf{R}_i} \int_0^\beta \mathrm{d}\tau_i. \tag{2.6}$$

2.1.2 One-particle Quantities

When considering a system where the Hamiltonian $\hat{\mathcal{H}}$ is time-independent, the (n)-particle Green's functions are invariant under a time shift $\tau_i - \tau_0$ and therefore not depending explicitly on the $2n$ times τ_i, but merely on time differences, since we can set $\tau_0 = \tau_{2n}$ [19]. Thus, for a time independent Hamiltonian $\hat{\mathcal{H}}$, we can choose the time arguments of the one-particle (1P) Green's function to be $\tau = \tau_1 - \tau_2$, 0 and write

$$G^{(1)}_{\sigma_1\sigma_2}(\tau, 0) =: G^{(1)}_{\sigma_1\sigma_2}(\tau). \tag{2.7}$$

The Fourier transform of the 1P Green's function $G^{(1)}_{\sigma_1\sigma_2}(\nu_1, \nu_2)$ will now also depend only on one Matsubara frequency $G^{(1)}_{\sigma_1\sigma_2}(\nu)$. If $\hat{\mathcal{H}}$ is further invariant under SU(2)-transformations (e.g., paramagnetic systems) and we consider conservation of spin (i.e. $\sigma_1 = \sigma_2$), then the 1P Green's function is also independent of σ_i [19] and can be redefined as

$$G(\nu) \ \delta_{\sigma_1\sigma_2} \coloneqq G^{(1)}_{\sigma_1\sigma_2}(\nu). \tag{2.8}$$

To give an explicit example, let us consider the Hamiltonian of a single fermionic orbital state $\hat{\mathcal{H}}_0 = \epsilon_0 \sum_\sigma \hat{c}^\dagger_\sigma \hat{c}_\sigma$, isolated, and of energy ϵ_0. The Green's function expressed in terms of Matsubara frequencies reads:

$$G^0(\nu) = \frac{1}{\mathrm{i}\nu - \epsilon_0}. \tag{2.9}$$

For a lattice of non-interacting fermions with dispersion relation $\epsilon_\mathbf{k}$, Hamiltonian $\hat{\mathcal{H}}_0 = \sum_{\mathbf{k},\sigma} \epsilon_\mathbf{k} \ \hat{c}^\dagger_{\mathbf{k}\sigma} \hat{c}_{\mathbf{k}\sigma}$, and non-fixed number of particles, we will instead obtain [16]

$$G^0_\mathbf{k}(\nu) = \frac{1}{\mathrm{i}\nu + \mu - \epsilon_\mathbf{k}}. \tag{2.10}$$

The superscript zero of $G^0(\nu)$ shall indicate that the Green's functions in Eq. (2.9, 2.10) describe non-interacting particles. In the general case, however, in the presence of an interaction term $\hat{\mathcal{V}}$ (e.g. $\hat{\mathcal{V}} = U_{ijkl}\ \hat{c}_i^\dagger \hat{c}_j^\dagger \hat{c}_k \hat{c}_l$) in $\hat{\mathcal{H}}$, the 1P Green's function cannot be expressed analytically. One usually calculates such quantities by performing a perturbation expansion in $\hat{\mathcal{V}}$ and expresses the full Green's function $G(\nu)$ of the interacting Hamiltonian $\hat{\mathcal{H}}$ by means of the non-interacting Green's function $G^0(\nu)$ of $\hat{\mathcal{H}}_0$. Thereby we take advantage of the very useful Feynman diagrammatic technique, which is described in great detail in Refs. [16, 17]. In a nutshell: Feynman diagrams are a diagrammatic representation of the terms in the perturbation expansion. Each non-interacting/interacting Green's function $G^0(\nu)/G(\nu)$ is represented by

$$G^0_{\mathbf{k}}(\nu) = \quad G_{\mathbf{k}}(\nu) = \tag{2.11}$$

and each interaction with

$$U_{ijkl}\ \hat{c}_i^\dagger \hat{c}_j^\dagger \hat{c}_k \hat{c}_l = \ . \tag{2.12}$$

We can think of each line in a Feynman diagram as a propagating particle and each node as scattering event. On every node the sum of frequencies and momenta must be conserved. With this diagrammatic representation, one can show that each disconnected diagram, will be cancelled by the denominator Z of Eq. (2.2). Further, $G_{\mathbf{k}}(\nu)$, consisting of only connected diagrams, can be separated into two classes of diagrams: (i) those which can be split by cutting one line of the diagram (1P-reducible) – which essentially represent a repetition of lower order processes – or those which cannot be split by cutting a fermionic line (1P-irreducible). The latter class – after amputating the external *legs* – defines the very important concept of the self-energy $\Sigma_{\mathbf{k}}(\nu)$:

$$= \quad + \quad + \ \ldots\ . \tag{2.13}$$

Thus, for the expansion of $G_{\mathbf{k}}(\nu)$ we can write

$$= \quad + \quad + \quad + \ \ldots\ , \tag{2.14a}$$

$$\text{or} \quad G_{\mathbf{k}}(\nu) = G^0_{\mathbf{k}}(\nu) + G^0_{\mathbf{k}}(\nu)\Sigma_{\mathbf{k}}(\nu)G^0_{\mathbf{k}}(\nu) + \ \ldots\ . \tag{2.14b}$$

This geometric series leads eventually to the Dyson-equation

$$G_{\mathbf{k}}(\nu) = G^0_{\mathbf{k}}(\nu) + G^0_{\mathbf{k}}(\nu)\Sigma_{\mathbf{k}}(\nu)G_{\mathbf{k}}(\nu), \tag{2.15}$$

which using the the explicit expression (2.10) reads

$$G_{\mathbf{k}}(\nu) = \frac{1}{\mathrm{i}\nu + \mu - \epsilon_{\mathbf{k}} - \Sigma_{\mathbf{k}}(\nu)}. \tag{2.16}$$

The difficult part of the calculation is now hidden in the self-energy $\Sigma_{\mathbf{k}}(\nu)$. Here, the physical effect of the interaction term $\hat{\mathcal{V}}$ on the Green's function appears in the substitution of $\epsilon_{\mathbf{k}} \to \epsilon_{\mathbf{k}} + \Sigma_{\mathbf{k}}(\nu)$. By expanding $\Sigma_{\mathbf{k}}(\nu)$ near the Fermi-surface

$$\Sigma_{\mathbf{k}}(\nu) \simeq\ \Sigma_{\mathbf{k}}(0) + \mathrm{i}\nu \left.\frac{\partial \Sigma_{\mathbf{k}}(\nu)}{\partial \nu}\right|_0 + \ldots\ , \tag{2.17}$$

we can reformulate the 1P Green's function as

$$G_{\mathbf{k}}(\nu) \simeq \frac{Z}{\mathrm{i}\nu + \mu - \widetilde{\epsilon_{\mathbf{k}}} + \mathrm{i}\gamma} + \dots \ . \tag{2.18}$$

This expression resembles closely the 1P Green's function of the free particle, but now with a renormalization factor $Z = (1 - \partial\Sigma_{\mathbf{k}}(\nu)/\partial\nu \,\big|_0)^{-1}$, finite lifetime $\gamma = -Z \,\mathrm{Im}\,\Sigma_{\mathbf{k}}(0)$, and shifted dispersion $\widetilde{\epsilon_{\mathbf{k}}} - \mu = Z(\epsilon_{\mathbf{k}} - \mu + \mathrm{Re}\,\Sigma_{\mathbf{k}}(0))$. The finite lifetime can be motivated heuristically, by substituting $\mathrm{e}^{-\mathrm{i}\epsilon_{\mathbf{k}}t} \to \mathrm{e}^{-\mathrm{i}\widetilde{\epsilon_{\mathbf{k}}}t}\mathrm{e}^{-\gamma t}$, for $\gamma > 0$ in the plane wave expression of the non-interacting Green's function expressed in the real time-domain.

Eq. (2.18) describes coherent excitations (called *quasi-particles*) in a Fermi-liquid: for low temperatures and in the metallic regime, when γ is small enough, they behave like independent particles with an effective mass [18]

$$m^* = \frac{m}{Z}\left(1 + \frac{\partial\Sigma_{\mathbf{k}}(0)}{\partial\epsilon_{\mathbf{k}}}\bigg|_{\mathbf{k}_F}\right)^{-1}. \tag{2.19}$$

Hence, Eq. (2.16) turns out to have two major advantages: (i) in the calculation less diagrams have to be considered compared to the *direct* calculation of the 1P Green's function and (ii) since Eq. (2.18) connects the self-energy to more physical *intuitive* quantities $\widetilde{\epsilon_{\mathbf{k}}}, Z, \gamma, m^*$, it is more convenient for developing and applying approximation schemes.

2.1.3 Two-particle Quantities

At the two-particle level, the quantity for us more interesting is not the two-particle (2P) Green's function $G^{(2)}_{\sigma_1\sigma_2\sigma_3\sigma_4}(\tau_1, \tau_2, \tau_3, \tau_4)$, but rather the generalised susceptibility $\chi_{\sigma_1\sigma_2\sigma_3\sigma_4}(\tau_1, \tau_2, \tau_3, \tau_4)$. The reason lies in the more direct physical interpretation of this quantity, as we shall see in the following.

The generalised susceptibility is defined with the 2P and 1P Green's functions as

$$\chi_{\sigma_1\sigma_2\sigma_3\sigma_4}(\tau_1, \tau_2, \tau_3, \tau_4) \coloneqq G^{(2)}_{\sigma_1\sigma_2\sigma_3\sigma_4}(\tau_1, \tau_2, \tau_3, \tau_4) - G^{(1)}_{\sigma_1\sigma_2}(\tau_1, \tau_2)G^{(1)}_{\sigma_3\sigma_4}(\tau_3, \tau_4). \tag{2.20}$$

As previously mentioned, if the Hamiltonian $\hat{\mathcal{H}}$ of the system is time-independent, we can omit one time argument of $\chi_{\sigma_1\sigma_2\sigma_3\sigma_4}(\tau_1, \tau_2, \tau_3, \tau_4)$ by shifting τ_4 to 0. Then, the Fourier transform of the generalised susceptibility χ depends only on three fermionic Matsubara frequencies ν_1, ν_2, ν_3, consistent with the energy conservation of the problem. In general – especially for relating the formalism to the definition of physical quantities – it is more convenient to switch to either the so-called particle-hole (ph) or the particle-particle (pp) notation, which read

$$\begin{aligned} ph: \quad & \nu_1 = \nu && pp: \quad & \nu_1 = \nu \\ & \nu_2 = \nu + \omega && & \nu_2 = \omega - \nu' \\ & \nu_3 = \nu' + \omega && & \nu_3 = \omega - \nu \\ & (\nu_4 = \nu') && & (\nu_4 = \nu'), \end{aligned} \tag{2.21}$$

where ω is a bosonic Matsubara (transfer) frequency and ν, ν' are fermionic ones. The term ph-notation arises from the Feynman diagrammatic of the generalised susceptibility. If we consider a generic diagram of χ in the ph-notation, then we can think of it, as a scattering event between an incoming quasi-particle $\longrightarrow$ with energy $\nu + \omega$ and a hole or antiparticle $\longleftarrow$ with energy $-\nu$, transferring the energy ω. For the pp-notation the same physical process is interpreted as scattering event between two quasi-particles with energy $\omega - \nu' \longrightarrow$ and $\nu' \longrightarrow$ [19]. In momentum space this would correspond to

Symmetry	Relation
Complex conjugation	$(\chi^{\nu\nu'\omega}_{ph,\sigma\sigma'})^* = \chi^{(-\nu')(-\nu)(-\omega)}_{ph,\sigma'\sigma} \overset{\mathrm{SU(2)}}{=} \chi^{(-\nu')(-\nu)(-\omega)}_{ph,\sigma\sigma'}$
SU(2)-symmetry	$\chi^{\nu\nu'\omega}_{ph,\sigma\sigma'} = \chi^{\nu\nu'\omega}_{ph,(-\sigma)(-\sigma')} = \chi^{\nu\nu'\omega}_{ph,\sigma'\sigma}$
Time reversal symmetry	$\chi^{\nu\nu'\omega}_{ph,\sigma\sigma'} = \chi^{\nu'\nu\ \omega}_{ph,\sigma'\sigma} \overset{\mathrm{SU(2)}}{=} \chi^{\nu'\nu\ \omega}_{ph,\sigma\sigma'}$
Particle-hole symmetry	$(\chi^{\nu\nu'\omega}_{ph,\sigma\sigma'})^* = \chi^{\nu\nu'\omega}_{ph,\sigma\sigma'}$

Table 2.1: Symmetry relations for the susceptibilities in *ph*-notation [19].

looking at the same scattering event in different reference systems (e.g. laboratory vs. centre of mass).

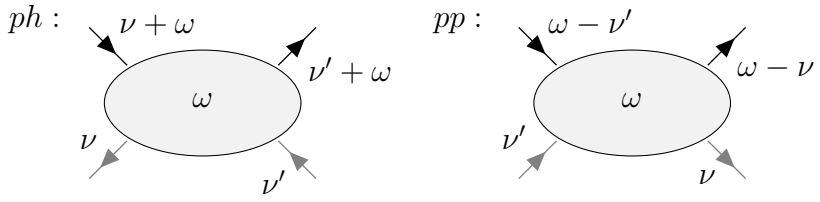

(2.22)

The choice between these formally equivalent formulations is dictated by the specific problem/quantity under investigation. Further invariance under SU(2)-transformations allows for additional simplifications of Eq. (2.20) [19]. The generalised susceptibility, thus, does no longer depend on four spins independently, but rather just on two degrees of freedom:

$$\chi_{\sigma_1\sigma_2\sigma_3\sigma_2} = \chi_{\sigma\sigma\sigma'\sigma'}{}^{1} =: \chi_{\sigma\sigma'}. \tag{2.23}$$

With the considerations made above, we obtain the Fourier transform of the generalised susceptibility in *ph*-notation as:

$$\begin{aligned}\chi^{\nu\nu'\omega}_{ph,\sigma\sigma'} = &\int_0^\beta \mathrm{d}\tau_1\mathrm{d}\tau_2\mathrm{d}\tau_3\ \mathrm{e}^{-\mathrm{i}\nu\tau_1}\mathrm{e}^{\mathrm{i}(\nu+\omega)\tau_2}\mathrm{e}^{-\mathrm{i}(\nu'+\omega)\tau_3}\\ &\times\big\{\langle\mathcal{T}\hat{c}^\dagger_\sigma(\tau_1)\hat{c}_\sigma(\tau_2)\hat{c}^\dagger_{\sigma'}(\tau_3)\hat{c}_{\sigma'}(0)\rangle\\ &-\langle\mathcal{T}\hat{c}^\dagger_\sigma(\tau_1)\hat{c}_\sigma(\tau_2)\rangle\ \langle\mathcal{T}\hat{c}^\dagger_{\sigma'}(\tau_3)\hat{c}_{\sigma'}(0)\rangle\big\}.\end{aligned} \tag{2.24}$$

The susceptibilities in the *ph*-notation fulfil certain properties stemming from the symmetries of the system, a subset of them are summarized in Tab. 2.1 [19]. These are evidently of great importance for the correct description of the physical properties.

For **k**-dependent Green's functions the Fourier transform of the generalised susceptibility will read [6]

$$\chi^{\nu\nu'\omega}_{ph,\sigma\sigma',\mathbf{k}\mathbf{k}'\mathbf{q}} = G^{(2)\nu\nu'\omega}_{\sigma\sigma',\mathbf{k}\mathbf{k}'\mathbf{q}} - \beta G_{\mathbf{k}}(\nu)G_{\mathbf{k}'}(\nu')\delta_{\omega 0}\delta_{\mathbf{q}\mathbf{0}}, \tag{2.25}$$

[1] A different possibility would be $\chi_{\sigma\sigma'\sigma'\sigma}$, which can be derived from $\chi_{\sigma\sigma\sigma'\sigma'}$ by a permutation of the fermionic operators and by considering the cyclic property of the trace [19].

where the momentum $\mathbf{q}$ is associated with the bosonic Matsubara frequency ω and $\mathbf{k}$, $\mathbf{k}'$ with the fermionic Matsubara frequencies ν, ν', respectively.

The charge "c" and spin "s" components of the generalised susceptibility are then defined as

$$\chi_{c,\mathbf{kk'q}}^{\nu\nu'\omega} = \chi_{ph,\uparrow\uparrow,\mathbf{kk'q}}^{\nu\nu'\omega} + \chi_{ph,\uparrow\downarrow,\mathbf{kk'q}}^{\nu\nu'\omega}, \tag{2.26a}$$

$$\chi_{s,\mathbf{kk'q}}^{\nu\nu'\omega} = \chi_{ph,\uparrow\uparrow,\mathbf{kk'q}}^{\nu\nu'\omega} - \chi_{ph,\uparrow\downarrow,\mathbf{kk'q}}^{\nu\nu'\omega}. \tag{2.26b}$$

In SU(2)-symmetric systems, this corresponds to *diagonalizing* the Bethe-Salpeter equations in the spin indices (see Eqs. (2.35) below and Ref. [21]).

From these quantities one can calculate the corresponding physical susceptibilities by performing the summation over all fermionic variables

$$\chi_{\mathbf{q}}^{r}(\omega) = \frac{2}{\beta^2} \sum_{\substack{\nu\nu' \\ \mathbf{kk'}}} \chi_{r,\mathbf{kk'q}}^{\nu\nu'\omega} \quad \text{with} \quad r = c, s.^2 \tag{2.27}$$

$\chi_{\mathbf{q}}^{r}(\omega)$ are the auto-correlation functions of the physical observables $\hat{n}_{\mathbf{q}}/\hat{s}_{\mathbf{q}}^{z} = \hat{n}_{\mathbf{q},\uparrow} \pm \hat{n}_{\mathbf{q},\downarrow}$, with $\hat{n}_{\mathbf{q},\sigma} = \sum_{\mathbf{k}} \hat{c}_{\mathbf{k},\sigma}^{\dagger} \hat{c}_{\mathbf{k}+\mathbf{q},\sigma}$ [4, 19]:

$$\begin{aligned} \chi_{\mathbf{q}}^{c}(\omega) = &\int_0^{\beta} \mathrm{d}\tau \; \mathrm{e}^{\mathrm{i}\omega\tau} \left\langle [\hat{n}_{\mathbf{q},\uparrow}(\tau) + \hat{n}_{\mathbf{q},\downarrow}(\tau)][\hat{n}_{\mathbf{q},\uparrow}(0) + \hat{n}_{\mathbf{q},\downarrow}(0)] \right\rangle \\ &- \beta\delta_{\omega 0}\delta_{\mathbf{q0}} \left\langle \hat{n}_{\mathbf{q},\uparrow} + \hat{n}_{\mathbf{q},\downarrow} \right\rangle^2, \end{aligned} \tag{2.28a}$$

$$\begin{aligned} \chi_{\mathbf{q}}^{s}(\omega) = &\int_0^{\beta} \mathrm{d}\tau \; \mathrm{e}^{\mathrm{i}\omega\tau} \left\langle [\hat{n}_{\mathbf{q},\uparrow}(\tau) - \hat{n}_{\mathbf{q},\downarrow}(\tau)][\hat{n}_{\mathbf{q},\uparrow}(0) - \hat{n}_{\mathbf{q},\downarrow}(0)] \right\rangle \\ &- \beta\delta_{\omega 0}\delta_{\mathbf{q0}} \left\langle \hat{n}_{\mathbf{q},\uparrow} - \hat{n}_{\mathbf{q},\downarrow} \right\rangle^2. \end{aligned} \tag{2.28b}$$

For $\omega = 0$ one obtains the *static* susceptibility, whereas by performing the analytical continuation $\mathrm{i}\omega \to \Omega + \mathrm{i}0^{+}$ the linear response function in dependence of real frequencies can be calculated. As the linear response function gives the response of the system upon external perturbation (up to first order), this quantity is directly related to spectroscopic experimental measurements, under the assumption that the electronic model of our choice is a good approximation for a real material.

To calculate the generalised susceptibility in a diagrammatic expansion, we will first decompose $\chi_{r,\mathbf{kk'q}}^{\nu\nu'\omega}$ into two parts [6, 19]

$\chi =$ 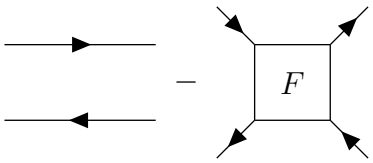 (2.29a)

$$\chi_{r,\mathbf{kk'q}}^{\nu\nu'\omega} = \chi_{0,\mathbf{kk'q}}^{\nu\nu'\omega} - G_{\mathbf{k}}(\nu) G_{\mathbf{k}+\mathbf{q}}(\nu+\omega) F_{r,\mathbf{kk'q}}^{\nu\nu'\omega} G_{\mathbf{k}'}(\nu') G_{\mathbf{k}'+\mathbf{q}}(\nu'+\omega). \tag{2.29b}$$

The first term

$$\chi_{0,\mathbf{kk'q}}^{\nu\nu'\omega} \coloneqq -\beta G_{\mathbf{k}}(\nu) G_{\mathbf{k}+\mathbf{q}}(\nu+\omega) \delta_{\nu\nu'} \delta_{\mathbf{kk'}} \tag{2.30}$$

is referred to as *bubble* contribution and describes the *independent* propagation of the particle and hole. For a system of non-interacting particles $\hat{\mathcal{H}}_0 = \sum_{\mathbf{k},\sigma} \epsilon_{\mathbf{k}} \; \hat{c}_{\mathbf{k}\sigma}^{\dagger} \hat{c}_{\mathbf{k}\sigma}$, the

[2] For a more direct comparison with the compressibility $\kappa \propto \partial n/\partial\mu$, considered later in this thesis we have included an additional factor 2 coming from the spin summation directly in the definitions of our physical susceptibilities, differently from the convention used in Refs. [6, 10, 19, 20, 22].

generalised susceptibility is given by just by this expression[3]

$$\chi^{\nu\nu'\omega}_{\sigma\sigma',\mathbf{k}\mathbf{k}'\mathbf{q}} = -\beta G^0_{\mathbf{k}}(\nu) G^0_{\mathbf{k}+\mathbf{q}}(\nu+\omega)\delta_{\nu\nu'}\delta_{\sigma\sigma'}\delta_{\mathbf{k}\mathbf{k}'} = \chi^{\nu\nu'\omega}_{0,\mathbf{k}\mathbf{k}'\mathbf{q}}\delta_{\sigma\sigma'}. \tag{2.31}$$

The second diagram in Eq. (2.29) describes the particle-hole scattering processes, where $F^{\nu\nu'\omega}_{r,\mathbf{k}\mathbf{k}'\mathbf{q}}$ can be interpreted, physically, as scattering amplitude for interacting particles [17]. We also recall that the discontinuity between the static ($\omega = 0,\ \mathbf{q} \to 0$) and the dynamic limit ($\mathbf{q} = 0,\ \omega \to 0$) of Eq. (2.29b) allows to draw a direct connection between the Fermi liquid parameters and the 2P vertex F [23]. Since our diagrams are now constructed from the full Green's function $G_{\mathbf{k}}(\nu) =$, we have to be careful not to count the same contributions twice. Therefore, we just consider *skeleton diagrams*, i.e. diagrams where internal lines do not have the same topological structure as the self-energy $\Sigma_{\mathbf{k}}(\nu)$ in Eq. (2.13).

To express $\chi^{\nu\nu'\omega}_{r,\mathbf{k}\mathbf{k}'\mathbf{q}}$ by means of $\chi^{\nu\nu'\omega}_{0,\mathbf{k}\mathbf{k}'\mathbf{q}}$ in the perturbation expansion, we apply the same diagrammatic technique as for the 1P quantities, by dividing the full scattering diagram $F^{\nu\nu'\omega}_{r,\mathbf{k}\mathbf{k}'\mathbf{q}}$ into reducible and irreducible contributions. However, there is some ambiguity to the term of 2P reducibility. $F^{\nu\nu'\omega}_{r,\mathbf{k}\mathbf{k}'\mathbf{q}}$ can be split into 2P reducible and irreducible diagrams of three topological distinct channels: ph, vertical particle-hole ($\overline{ph}$), and pp. We denote diagrams which are reducible in channel l by $\Phi^{\nu\nu'\omega}_{l,r,\mathbf{k}\mathbf{k}'\mathbf{q}}$ and diagrams which are fully irreducible by $\Lambda^{\nu\nu'\omega}_{r,\mathbf{k}\mathbf{k}'\mathbf{q}}$. Therefore we find the unique decomposition [6, 19]

$$F^{\nu\nu'\omega}_{r,\mathbf{k}\mathbf{k}'\mathbf{q}} = \Lambda^{\nu\nu'\omega}_{r,\mathbf{k}\mathbf{k}'\mathbf{q}} + \Phi^{\nu\nu'\omega}_{ph,r,\mathbf{k}\mathbf{k}'\mathbf{q}} + \Phi^{\nu\nu'\omega}_{\overline{ph},r,\mathbf{k}\mathbf{k}'\mathbf{q}} + \Phi^{\nu\nu'\omega}_{pp,r,\mathbf{k}\mathbf{k}'\mathbf{q}} \tag{2.32a}$$

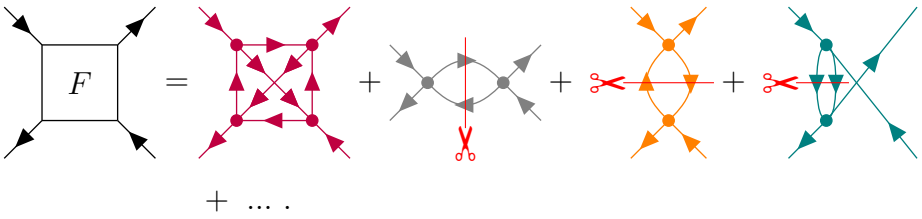

(2.32b)

In Eq. (2.32b) we depicted four exemplary diagrams of $F^{\nu\nu'\omega}_{r,\mathbf{k}\mathbf{k}'\mathbf{q}}$ and coloured them like the corresponding contributing term $\Phi^{\nu\nu'\omega}_{l,r,\mathbf{k}\mathbf{k}'\mathbf{q}}$ or $\Lambda^{\nu\nu'\omega}_{r,\mathbf{k}\mathbf{k}'\mathbf{q}}$ in Eq. (2.32a). The 2P reducibility – which corresponds to cutting two fermionic propagators – in channel l of the diagrams is indicated by a red cutting line  . Such classification corresponds to the so-called parquet equations.

However, we can also divide $F^{\nu\nu'\omega}_{r,\mathbf{k}\mathbf{k}'\mathbf{q}}$ into only two parts restricting to one channel l

$$F^{\nu\nu'\omega}_{r,\mathbf{k}\mathbf{k}'\mathbf{q}} = \Gamma^{\nu\nu'\omega}_{l,r,\mathbf{k}\mathbf{k}'\mathbf{q}} + \Phi^{\nu\nu'\omega}_{l,r,\mathbf{k}\mathbf{k}'\mathbf{q}}, \tag{2.33}$$

where we introduced the irreducible diagrams in the selected channel l ($\Gamma^{\nu\nu'\omega}_{l,r,\mathbf{k}\mathbf{k}'\mathbf{q}}$). Now, similar to the 1P case, we can separate the generalised susceptibility $\chi^{\nu\nu'\omega}_{r,\mathbf{k}\mathbf{k}'\mathbf{q}}$in two distinct classes of diagrams, either reducible in channel l, or irreducible in l and obtain [19]

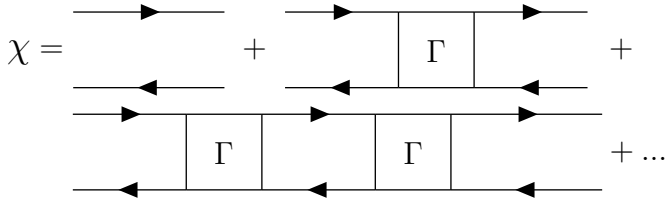

(2.34a)

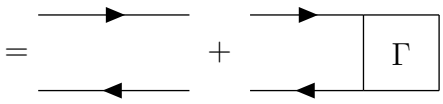

(2.34b)

[3]Note that $\chi^{\nu\nu'\omega}_{0,\mathbf{k}\mathbf{k}'\mathbf{q}}$ depends in general on $G_{\mathbf{k}}(\nu)$ and not on $G^0_{\mathbf{k}}(\nu)$.

Which is the diagrammatic expression of the Bethe-Salpeter equations [19, 20]

$$\chi^{\nu\nu'\omega}_{c,\mathbf{k}\mathbf{k}'\mathbf{q}} = \chi^{\nu\nu'\omega}_{0,\mathbf{k}\mathbf{k}'\mathbf{q}} - \frac{1}{\beta^2}\sum_{\substack{\nu_1\nu_2\\ \mathbf{k}_1\mathbf{k}_2}} \chi^{\nu\nu_1\omega}_{0,\mathbf{k}\mathbf{k}_1\mathbf{q}}\Gamma^{\nu_1\nu_2\omega}_{c,\mathbf{k}_1\mathbf{k}_2\mathbf{q}}\chi^{\nu_2\nu'\omega}_{c,\mathbf{k}_2\mathbf{k}'\mathbf{q}}, \tag{2.35a}$$

$$\chi^{\nu\nu'\omega}_{s,\mathbf{k}\mathbf{k}'\mathbf{q}} = \chi^{\nu\nu'\omega}_{0,\mathbf{k}\mathbf{k}'\mathbf{q}} - \frac{1}{\beta^2}\sum_{\substack{\nu_1\nu_2\\ \mathbf{k}_1\mathbf{k}_2}} \chi^{\nu\nu_1\omega}_{0,\mathbf{k}\mathbf{k}_1\mathbf{q}}\Gamma^{\nu_1\nu_2\omega}_{s,\mathbf{k}_1\mathbf{k}_2\mathbf{q}}\chi^{\nu_2\nu'\omega}_{s,\mathbf{k}_2\mathbf{k}'\mathbf{q}}, \tag{2.35b}$$

with [20]

$$\Gamma^{\nu\nu'\omega}_{c,\mathbf{k}\mathbf{k}'\mathbf{q}} = \Gamma^{\nu\nu'\omega}_{ph,\uparrow\uparrow,\mathbf{k}\mathbf{k}'\mathbf{q}} + \Gamma^{\nu\nu'\omega}_{ph,\uparrow\downarrow,\mathbf{k}\mathbf{k}'\mathbf{q}}, \tag{2.36a}$$

$$\Gamma^{\nu\nu'\omega}_{s,\mathbf{k}\mathbf{k}'\mathbf{q}} = \Gamma^{\nu\nu'\omega}_{ph,\uparrow\uparrow,\mathbf{k}\mathbf{k}'\mathbf{q}} - \Gamma^{\nu\nu'\omega}_{ph,\uparrow\downarrow,\mathbf{k}\mathbf{k}'\mathbf{q}}. \tag{2.36b}$$

They are the 2P analogion of Eq. (2.15).

2.2 The Hubbard Model

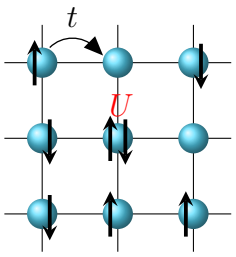

FIG. 2.1: Illustration of the Hubbard model on a square-lattice, on each lattice site electrons – indicated by arrows – interact with U. t determines the probability of electron-hopping between the lattice sites.

The Hubbard model is one of the most fundamental Hamiltonians to describe electronic correlation effects and study the delicate balance between the kinetic and potential energy of interacting electrons.

It describes a lattice, where on each site a localised orbital is located, and electrons can hop from one lattice site to another. In the simplest (one band) case, the Pauli exclusion principle allows a maximum of two electrons on each site. Whenever two electrons occupy it simultaneously, they are subject to the mutual repulsion of interaction strength U. All other (non-local) contributions of the Coulomb interaction are neglected.

A schematic illustration is shown in Fig. 2.1. The Hamiltonian $\hat{\mathcal{H}}$ of the Hubbard model reads explicitly

$$\hat{\mathcal{H}} - \mu\hat{\mathcal{N}} = -t\sum_{i\neq j,\sigma}\hat{c}^\dagger_{i\sigma}\hat{c}_{j\sigma} - \mu\sum_{i,\sigma}\hat{n}_{i\sigma} + U\sum_i \hat{n}_{i\uparrow}\hat{n}_{i\downarrow}, \tag{2.37}$$

where t is the hopping parameter, $\hat{c}^{(\dagger)}_{i\sigma}$ the annihilation (creation) operator at each lattice site i and $\hat{n}_{i\sigma} = \hat{c}^\dagger_{i\sigma}\hat{c}_{i\sigma}$ the number operator for electrons with spin σ on site i ($\hat{n}_{i\sigma} = 0$ or 1). For $U = 0$ the Hubbard model obviously reduces to the non-interacting electron gas of the lattice

$$\hat{\mathcal{H}}_{U=0} = -t\sum_{i\neq j,\sigma}\hat{c}^\dagger_{i\sigma}\hat{c}_{j\sigma} = \sum_{\mathbf{k},\sigma}\epsilon_{\mathbf{k}}\ \hat{c}^\dagger_{\mathbf{k}\sigma}\hat{c}_{\mathbf{k}\sigma}. \tag{2.38}$$

In this thesis we will consider the Hubbard model on a square-lattice, the dispersion relation of the free electron gas can be obtained by a Fourier transform of the hoping term in Eq. (2.37) and is given by

$$\epsilon_{\mathbf{k}} = -2t(\cos k_x a + \cos k_y a), \tag{2.39}$$

where $a = 1$ is the lattice spacing. The hopping parameter in our model is set to $t = 1/4$.

2.3 Dynamical Mean Field Theory (DMFT)

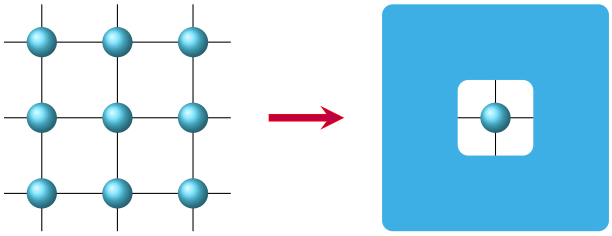

FIG. 2.2: DMFT maps the Hubbard model on an effective single site problem in a time-dependent mean field, i.e. it represents a quantum extension of a classical mean-field approximation.

Despite being a relatively simple model of a solid, the Hubbard model is in general not analytically solvable (and in most cases not even numerically), thus for gaining some physical insight, one has to perform approximations. Our approximation of choice is the Dynamical Mean Field Theory (DMFT). In DMFT we map the Hubbard model onto an effective single site problem embedded in a time-dependent mean-field or auxiliary bath of electrons. This, which represents a quantum extension of the classical mean-field concept, corresponds physically to neglect all spatial correlations which are not completely local. Such an approximation becomes, thus, exact by taking the limit of large dimensionality[4] or large lattice connectivity [24]. Formally, DMFT correspond to replacing the action of the Hubbard model

$$S = \int_0^\beta \mathrm{d}\tau \left(\sum_{i,\sigma} \hat{c}^\dagger_{i\sigma}(\tau) \left(\frac{\mathrm{d}}{\mathrm{d}\tau} - \mu \right) \hat{c}_{i\sigma}(\tau) + \mathcal{H}\left(\hat{c}^\dagger_{i\sigma}(\tau), \hat{c}_{i\sigma}(\tau) \right) \right) \tag{2.40}$$

with an effective action of a quantum impurity model [4]

$$S_{\text{eff}} = -\int_0^\beta \mathrm{d}\tau \int_0^\beta \mathrm{d}\tau' \sum_\sigma \hat{c}^\dagger_{0\sigma}(\tau) \mathcal{G}_0^{-1}(\tau - \tau') \hat{c}_{0\sigma}(\tau') + U \int_0^\beta \mathrm{d}\tau \; \hat{n}_{0\uparrow}(\tau) \hat{n}_{0\downarrow}(\tau), \tag{2.41}$$

where $\mathcal{G}_0^{-1}(\tau - \tau')$ plays the role of the mean field and is the noninteracting Green's function of the effective single site ($\hat{c}^{(\dagger)}_{0\sigma}$), but not of the original lattice model. In DMFT a closed set of equations is obtained by relating the local quantities calculated from S_{eff} to the original lattice. For the limit of infinite dimensions d these equation will become exact[5], for finite d they represent an approximative solution. S_{eff} can be associated with

[4] In general this is a rather crude approximation for a two-dimensional lattice, however already in three dimensions this can be a good approximation for strong correlation [24]. Nevertheless, the study of DMFT in a two-dimensional lattice gives great insight in physical mechanisms and calculations of this system are less demanding in computational power.

[5] By taking the limit $d \to \infty$, the hopping parameter $t = t_{const}/\sqrt{2d}$ must be rescaled accordingly to ensure a non-trivial limit of the kinetic energy and density of states.

an auxiliary Hamiltonian of the Anderson impurity model (AIM) – i.e. a model of a local impurity ($\hat{c}^{(\dagger)}_{0\sigma}$) interacting with a bath of free electrons ($\hat{a}^{(\dagger)}_{l\sigma}$) –

$$\hat{\mathcal{H}}_{AIM} = \sum_{l,\sigma} \tilde{\epsilon}_l \hat{a}^\dagger_{l\sigma}\hat{a}_{l\sigma} + \sum_{l,\sigma} V_l \left(\hat{a}^\dagger_{l\sigma}\hat{c}_{0\sigma} + \hat{c}^\dagger_{0\sigma}\hat{a}_{l\sigma} \right) + U\hat{n}_{0\uparrow}\hat{n}_{0\downarrow}. \tag{2.42}$$

This can be verified by integrating out the free electrons ($\hat{a}^{(\dagger)}_{l\sigma}$) in the action of the AIM S_{AIM} [4]. In doing so one obtains Eq. (2.41) with

$$\begin{aligned} \mathcal{G}_0^{-1}(\nu) &= \mathrm{i}\nu + \mu - \Delta(\nu), \\ \Delta(\nu) &= \sum_l \frac{V_l^2}{\mathrm{i}\nu - \tilde{\epsilon}_l}. \end{aligned} \tag{2.43}$$

For the AIM various numerical solvers can be applied to calculate the interacting impurity Green's function $G_{AIM}(\nu)$ for a given $\mathcal{G}_0^{-1}(\nu)$. In practice, one starts typically with an initial guess of $\mathcal{G}_0^{-1}(\nu)$ for the calculations. Then, with $\mathcal{G}_0$ and $G_{AIM}(\nu)$ the self-energy can be calculated by

$$\Sigma(\nu) = \mathcal{G}_0^{-1}(\nu) - G_{AIM}^{-1}(\nu). \tag{2.44}$$

From the self-energy the lattice Green's function will be obtained through the Dyson equation of the lattice

$$G_{\mathbf{k}}(\nu) = \frac{1}{\mathrm{i}\nu - \epsilon_{\mathbf{k}} + \mu - \Sigma(\nu)}, \tag{2.45}$$

and a summation over the $\mathbf{k}$-space yields the (new) local Green's function of the lattice

$$G_{loc}(\nu) = \sum_{\mathbf{k}} G_{\mathbf{k}}(\nu), \tag{2.46}$$

which is then compared with the previously calculated $G_{AIM}(\nu)$ of the AIM. If they do not coincide,

$$\mathcal{G}_0^{\text{new}}(\nu) = [G_{loc}(\nu)]^{-1} + \Sigma(\nu) \tag{2.47}$$

gives a new input for the AIM solver. These calculations are repeated until convergence. This calculation procedure is shown in Fig. 2.3. Since the self-energy $\Sigma(\nu)$ of the lattice Green's function $G_{\mathbf{k}}(\nu)$ in Eq. (2.45) does not depend on the lattice momenta $\mathbf{k}$, DMFT can be in fact also understood as approximation of $\Sigma_{\mathbf{k}}(\nu) \approx \Sigma(\nu)$.

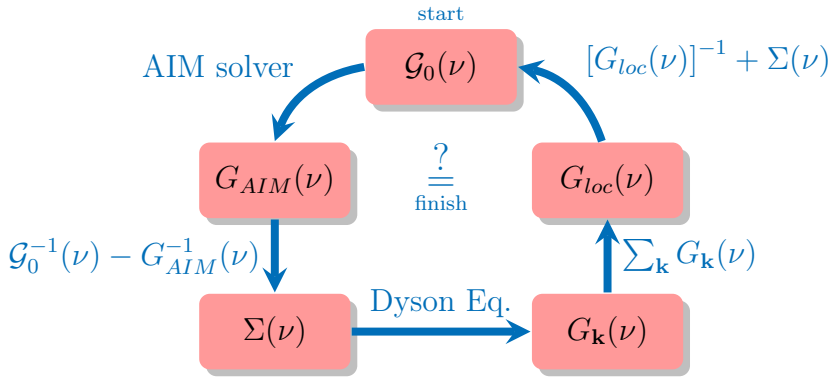

FIG. 2.3: Flow diagram of the DMFT algorithm.

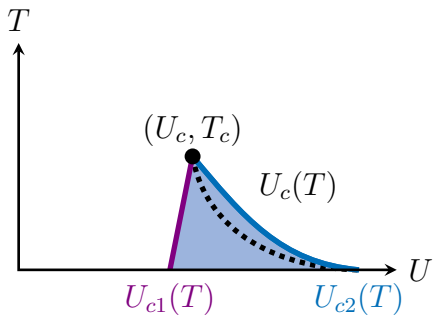

FIG. 2.4: Schematic plot of the Mott metal-insulator transition at half-filling ($n = 1,\ \mu = U/2$) in DMFT for the one band Hubbard model on the square-lattice. Violet line: bifurcation lines $U_{c1}(T)$; blue line: $U_{c2}(T)$; black dot: critical endpoint (U_c, T_c); dotted line: first order transition $U_c(T)$.

2.4 Mott Insulator Transition in DMFT

One great success of DMFT is the successful description of the Mott transition. The Mott transition is a metal-insulator transition (MIT) without a change in symmetry which is appearing e.g. in the paramagnetic-to-antiferromagnetic transition or the Peierls transition [2]. The Mott transition is driven by the mutual electron-electron repulsion in the localized d- and f- orbitals. This marks the difference with band insulators, where the insulating is caused by a complete filled valence band and a gap between the next empty band and the Fermi level, purely resulting from the Pauli principle and the influence of the ionic lattice potential and not by electron-electron interactions.

In the single-band Hubbard model, the Mott-transition is driven by the interaction U. If we consider the half filled

$$n = \left\langle \sum_{\sigma} \hat{n}_{i\sigma} \right\rangle = 1 \tag{2.48}$$

case, when $\mu = U/2$ and the model is *particle-hole* symmetric, increasing U – i.e. the energy cost of having double occupied sites – will eventually lead to a state where every lattice site is only occupied once (localized moments). When the energy cost for double occupation is too high hopping processes in the Hubbard model get completely supressed stabilising the Mott insulating phase.

In DMFT the MIT in the Hubbard model can be viewed, more formally, as bifurcation points of a functional of the local Green's function $G_{loc}(\nu)$ [25]. Then, the phase diagram of the Hubbard model (Fig. 2.4 at $n = 1$) displays a region where two coexisting solutions of the calculations, a metallic and insulating Green's function are obtained (delimited by the bifurcation lines $U_{c1}(T)$ and $U_{c2}(T)$). A first order transition $U_c(T)$ topped by a second order critical endpoint (U_c, T_c) – similar in many respects to the Van der Waals gas phase transition – takes place where the free energies of the two solutions cross.

2.5 Monte Carlo in Continuous Time Hybridization Expansion

Our DMFT calculations of the one- and two-particle quantities were performed with the *w2dynamic*-package [26]. *w2dynamics* is a continuous-time quantum Monte Carlo solver in the hybridization expansion (CT-HYB) for the AIM. For a detailed review on continuous

time quantum Monte Carlo (QMC) methods we refer the reader to the literature e.g. Ref. [27].

The basic idea of QMC in CT-HYB is to split the Hamiltonian of the AIM in Eq. (2.42) in two parts

$$\hat{\mathcal{H}}_{AIM} = \hat{\mathcal{H}}_{rest} + \hat{\mathcal{H}}_{hyb}, \tag{2.49}$$

the hybridization term

$$\hat{\mathcal{H}}_{hyb} = \sum_{l,\sigma} V_l \left(\hat{a}^\dagger_{l\sigma} \hat{c}_{0\sigma} + \hat{c}^\dagger_{0\sigma} \hat{a}_{l\sigma} \right) \tag{2.50}$$

and the rest $\hat{\mathcal{H}}_{rest}$ to expand the Green's function or e.g. the partition function $Z = \mathrm{Tr}\left(\mathrm{e}^{-\beta\hat{\mathcal{H}}}\right)$ in powers of $\hat{\mathcal{H}}_{hyb}$:

$$\begin{aligned} Z &= \mathrm{Tr}\left(\mathcal{T} \mathrm{e}^{-\beta\hat{\mathcal{H}}_{rest}} \exp\left(-\int_0^\beta \mathrm{d}\tau \hat{\mathcal{H}}_{hyb}(\tau) \right) \right) \\ &= \sum_m (-1)^m \int_0^\beta \mathrm{d}\tau_1 ... \int_{\tau_{m-1}}^\beta \mathrm{d}\tau_m \, \mathrm{Tr}\left(\mathrm{e}^{-\beta\hat{\mathcal{H}}_{rest}} \hat{\mathcal{H}}_{hyb}(\tau_m) \times ... \times \hat{\mathcal{H}}_{hyb}(\tau_1) \right). \end{aligned} \tag{2.51}$$

The trace Tr is then evaluated by the Monte Carlo method by sampling over all orders m, all distinct configurations (topological distinct Feynman diagrams), and all times $\tau_1 ... \tau_m$ in the same calculation [27].

Chapter 3

Uniform and Local Response in DMFT

"You know what's weird? Day by day, nothing seems to change, but pretty soon...everything's different."
-Bill Watterson

In this chapter, we set the stage for our theoretical considerations motivating the work presented in this thesis. In the first part we consider the charge compressibility and its behaviour in the proximity of the MIT of the Hubbard model, for single orbital systems as well as for multiorbital systems. The key equation of our study – the Bethe Salpeter Equation (BSE) in DMFT – is discussed afterwards, with a particular focus on its thermodynamic consistency. Thereafter, we introduce the topic of the vertex divergences occurring in all fundamental many-electron models and discuss the formal relation with the suppression of local fluctuations. Finally, in the last section, we illustrate a new physical scenario in which the occurrence of vertex divergencies in the charge section might induce a strong dichotomy between the local and the uniform response and even a thermodynamic instability towards a phase separation.

3.1 Charge Compressibility and the Landscape of the Mott Insulator Transition

The electronic isothermal compressibility or charge compressibility is defined as

$$\kappa = \frac{1}{n^2} \left. \frac{\partial n}{\partial \mu} \right|_T , \tag{3.1}$$

with n being the density and μ the chemical potential. An alternative formulation[1] of Eq. (3.1) – most commonly used for describing fluids – is given by $\kappa = -\frac{1}{V} \left. \frac{\partial V}{\partial P} \right|_{T,N}$.

The compressibility is proportional to the static charge susceptibility

$$\chi^c_{\mathbf{q}=\mathbf{0}}(\omega = 0) = \partial n / \partial \mu = \beta \big(\langle \hat{n}^2 \rangle - \langle \hat{n} \rangle^2 \big), \tag{3.2}$$

which measures the change of the density n in response of a variation of the chemical potential μ and is also the auto-correlation of n (for a proof see appendix 6.2). Hence, it is also a measure of the density fluctuations in the system. In the following we will drop the bosonic transfer frequency ω of the susceptibility and consider the static case only:

[1] The derivation of Eq. (3.1) from the well-known formula $\kappa = -\frac{1}{V} \left. \frac{\partial V}{\partial P} \right|_{T,N}$ is given in the appendix 6.1.

$\chi^c_{\mathbf{q}=\mathbf{0}}(\omega = 0) =: \chi^c_{\mathbf{q}=\mathbf{0}}$.

In the DMFT phase-diagram of the Hubbard model – which is schematically illustrated in Fig. 3.1 – also out of half filling ($n \neq 1$) a thermodynamic phase transition, with a coexistence region (blue shaded area) is found [14]. However, in this case (e.g. if $n < 1$) – unlike at half-filling (see Sec. 2.4) – no MIT takes place, instead one finds a phase transition between a (lower density) metal and a (higher density) bad metallic phase, which gradually becomes more insulating towards the Mott insulator at half-filling.

The charge susceptibility $\chi^c_{\mathbf{q}=\mathbf{0}}$ characterizes the thermodynamics of this phase transitions: $\chi^c_{\mathbf{q}=\mathbf{0}} = 0$ describes the Mott insulator, $\chi^c_{\mathbf{q}=\mathbf{0}} \to \infty$ a second-order transition or critical endpoint of a phase separation (blue dots)[2], and a discontinuity in $\chi^c_{\mathbf{q}=\mathbf{0}}$ a first-order transition. The transition is equivalent, to a large extent, to the Van der Waals liquid-gas transition: the metallic regime - corresponding to the Van der Waals gas phase – shows a fairly constant compressibility κ, while the insulating-like phase – the liquid phase – has nearly zero compressibility [29]. By going above the critical endpoints $T > T_c$ two phases change continuously into each other (crossover region).

By going closer to the critical endpoints, where $\chi^c_{\mathbf{q}=\mathbf{0}}$ and, thus, κ is diverging, also the correlation length ξ – a measure of the length over which the density on the different sites are correlated [30] – diverges. In this regime, $\chi^c_{\mathbf{q}}$ around $\mathbf{q} = \mathbf{0}$ behaves as predicted by the Ornstein-Zernike function [31]:

$$\chi^c_{\mathbf{q}} \simeq \frac{A}{\mathbf{q} + \xi^{-2}}. \tag{3.3}$$

Directly above ($T > T_c$) the critical endpoint(s) (dotted line in Fig. 3.1), out of half-filling, an enhancement of the compressibility has been indeed observed in DMFT [15]. However, we are interested to clarify here, how this enhancement in the compressibility is triggered on the level of two particle scattering processes. Instead, the increase in κ can be interpreted [15], to a given extent, as an attractive effect in a parameter region were a strong electronic repulsion – high interaction U – is prevalent.

Such an interpretation can be heuristically motivated by the random-phase-approximation (RPA), which simply replaces the irreducible vertex $\Gamma^{\nu\nu'\omega}_{c,\mathbf{kk'q}} \simeq U$ in the Bethe-Salpeter equation. Hence, Eq. (2.35a) can be solved straightforwardly for the physical susceptibility $\chi^c_{\mathbf{q}} = \frac{2}{\beta^2} \sum_{\substack{\nu\nu' \\ \mathbf{kk'}}} \chi^{\nu\nu'\omega=0}_{c,\mathbf{kk'q}}$:

$$\chi^c_{\mathbf{q}} = \frac{2\chi^0_{\mathbf{q}}}{1 + U\chi^0_{\mathbf{q}}}, \tag{3.4}$$

with $\chi^0_{\mathbf{q}} = \frac{1}{\beta^2} \sum_{\substack{\nu\nu' \\ \mathbf{kk'}}} \chi^{\nu\nu'\omega=0}_{0,\mathbf{kk'q}}$. Evidently an enhancement in this expression occurs only for an attractive $U \to -U$, which is not possible in our case since we are in a region where U is strongly repulsive.

[2] For a particle-hole symmetric Hubbard model – e.g. in the Bethe or in the unfrustrated square-lattice, directly at half-filling – no divergence in $\kappa \propto \chi^c_{\mathbf{q}=\mathbf{0}}$ is observed [14, 28].

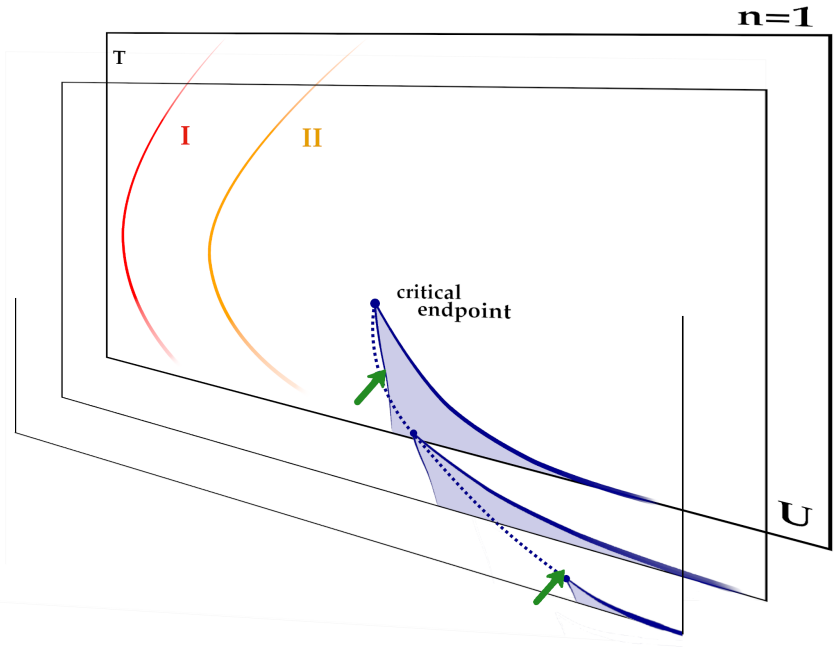

FIG. 3.1: Schematic phase diagram of the Hubbard model in DMFT. The different layers illustrate different filling (density) n, in the back $n = 1$ (half-filling) is depicted, the layers in the front show $n < 1$. In each layer one finds a coexisting region (shaded in blue) as a function of U and T, gradually shifted towards higher U_c away from half-filling and extending to smaller and smaller temperatures T_c. The blue dots illustrate the critical endpoints (U_c, T_c) of each layer. The blue dotted line connects the critical endpoints of each n. The green arrows show the parameter region were the calculations were performed, see chapter 4. The red (I) and the orange (II) line marks the position of the first two divergence lines of the irreducible vertex at half-filling, discussed in Sec. 3.4. Taken from Ref. [28].

3.2 Charge Compressibility in Multiorbital Systems

Thus far, we focused only on the single-band Hubbard Hamiltonian, however we can extend the physical phenomena described in our model by including multiple correlated orbitals on each lattice site. Such multiorbital Hubbard models can account for the description of transition-metals compounds (typically oxides) – with their localised $3d$-orbitals – and rare-earth elements, with localised $4f/5f$-orbitals [32, 33].

The general form of a multiorbital Hubbard Hamiltonians is [34]:

$$\hat{\mathcal{H}} = \sum_{ij,mm',\sigma} t_{ij}^{mm'} \hat{c}_{im\sigma}^{\dagger} \hat{c}_{jm'\sigma} + \sum_{i,mm'm''m''',\sigma\sigma'} U_{mm'm''m'''} \; \hat{c}_{im\sigma}^{\dagger} \hat{c}_{im'\sigma'}^{\dagger} \hat{c}_{im'''\sigma'} \hat{c}_{im''\sigma}, \tag{3.5}$$

where m, m', m'', m''' are orbital indices and i and j site indices. $U_{mm'm''m'''}$ represents the projection of the Coulomb (screened) interaction onto the localised orbitals and encodes several processes: additional to the mutual intra-orbital repulsion U of the electrons in the same orbital, also an inter-orbital repulsion U' between different orbitals is introduced. The Hund's effect in this materials – i.e. the tendency to first occupy different orbitals with electrons of the same spin – is encoded in the Hund's-coupling term J, which reduces the inter-orbital repulsion U' between different orbitals by $U' - J$ for identical spin [35, 36].

In general, the inter-orbital repulsion is expected to be smaller than the intra-orbital repulsion $U' < U$, if rotational invariance in a cubic lattice is considered: $U' = U - 2J$

[35, 36]. Further, also pair hopping and spin exchange between orbitals is included in Eq. (3.5).

The physics of this multiorbital model gets largely influenced by the interplay between the repulsion U – favouring single occupation – the Hund's exchange J – favouring large momenta as well as by the electron density. Out of half-filling (e.g. for integer filling $n = N/2 \pm 1$, where N is the number of correlated orbitals) for large U and low J eventually a Mott insulating-like metal is observed, where every site has the same electronic density and orbital double occupancy is suppressed.

On the other hand, for large J and small U an insulating phase is also observed, but now favouring high spin configurations on the lattice sites. This induces a charge disproportion (charge-density-wave-like structure), often called Hund's insulator[3]: orbitals are either fully single occupied (yielding a large momenta) or empty.

Directly at half-filling one cannot distinguish between this two insulating states, as the high-spin configuration corresponds also to the Mott state, instead, the critical point U_c of the Mott insulator is observed at much lower U values.

Out of half-filling for specific values of J e.g. $J = U/3$, one does instead find an intermediate metallic regime emerging by the competition between those two insulating states, where the interplay between U and J cancels the different insulating tendencies. This regime can survive even for very strong interaction and is called Hund's metal phase[36, 37].

For constant J/U near the Mott insulating state at half-filling, an enhancement of the compressibility κ has been observed – seemingly to occurring at the crossover region between a Hund's metal and a regular metal – eventually diverging at the border of a whole zone of phase instability (negative κ) [36, 38, 39].

Hence, also in multiorbital systems, the divergence of the charge compressibility out of half-filling is directly rooted in a parameter regime of strong interaction or correlation, whose effects might get further enhanced by the larger maximal size of local magnetic moment.

Throughout this work we will focus on the single-band Hubbard model. The goal is to gain also a deeper insight in these intriguing physical processes, which could be later useful for the interpretation of the multi-orbital cases.

3.3 Bethe-Salpeter Equation in DMFT

The Bethe-Salpeter equation (BSE) – here for the charge-channel –

$$\chi_{c,\mathbf{k}\mathbf{k}'\mathbf{q}}^{\nu\nu'\omega} = \chi_{0,\mathbf{k}\mathbf{k}'\mathbf{q}}^{\nu\nu'\omega} - \frac{1}{\beta^2} \sum_{\substack{\nu_1\nu_2 \\ \mathbf{k}_1\mathbf{k}_2}} \chi_{0,\mathbf{k}\mathbf{k}_1\mathbf{q}}^{\nu\nu_1\omega} \Gamma_{c,\mathbf{k}_1\mathbf{k}_2\mathbf{q}}^{\nu_1\nu_2\omega} \chi_{c,\mathbf{k}_2\mathbf{k}'\mathbf{q}}^{\nu_2\nu'\omega} \tag{3.6}$$

can be crucially simplified in the limit of infinite dimensions $d \to \infty$ (DMFT) [4, 40]: all the fully irreducible 2P diagrams become completely *local* $\Lambda_{r,\mathbf{k}\mathbf{k}'\mathbf{q}}^{\nu\nu'\omega} \to \Lambda_r^{\nu\nu'\omega}$, the irreducible vertex $\Gamma_{c,\mathbf{k}\mathbf{k}'\mathbf{q}}^{\nu\nu'\omega}$ instead displays still a residual momentum dependence[4] for special $\mathbf{k}$-points, however their relative measure in the summation over $\mathbf{k}$ in the Brillouin zone scales to zero in the limit of $d \to \infty$. Therefore, in DMFT we can replace the irreducible vertex

[3]The Hund's insulator displays some similarity to an insulator for attractive $-U$, here also a charge-density wave like structure is observed.

[4]For the $d = \infty$ hypercubic lattice, the momentum dependence is entering only through the quantity: $\lim_{d\to\infty} \frac{1}{d} \sum_{i=1}^{d} \cos k_i$, which is zero for a *generic* $\mathbf{k}$-vector, exept for special $\mathbf{k}$-points, such as $(0, 0, 0, \dots)^T$ or $(\pi, \pi, \pi, \dots)^T$ [4].

by a purely local quantity $\Gamma_c^{\nu\nu'\omega}$. Since we will consider the *static* limit ($\omega = 0$) for the susceptibility, we will drop the ω indices. With the considerations above we can rewrite the BSE in DMFT in the following form:

$$\chi_{c,\mathbf{q}}^{\nu\nu'} = \chi_{\mathbf{q}}^{0}(\nu)\,\delta_{\nu\nu'} - \chi_{\mathbf{q}}^{0}(\nu)\,\frac{1}{\beta^2}\sum_{\nu_1}\Gamma_c^{\nu\nu_1}\chi_{c,\mathbf{q}}^{\nu_1\nu'}, \tag{3.7}$$

with $\chi_{c,\mathbf{q}}^{\nu\nu'} = \sum_{\mathbf{k}\mathbf{k}'}\chi_{c,\mathbf{k}\mathbf{k}'\mathbf{q}}^{\nu\nu'}$ and $\chi_{\mathbf{q}}^{0}(\nu)\,\delta_{\nu\nu'} = \sum_{\mathbf{k}\mathbf{k}'}\chi_{0,\mathbf{k}\mathbf{k}'\mathbf{q}}^{\nu\nu'}$ calculated from the lattice Green's function: $\chi_{0,\mathbf{k}\mathbf{k}'\mathbf{q}}^{\nu\nu'} = -\beta G_{\mathbf{k}}(\nu)G_{\mathbf{k}+\mathbf{q}}(\nu)\delta_{\nu\nu'}\delta_{\mathbf{k}\mathbf{k}'}$. The $\mathbf{q}$-dependence of the susceptibility $\chi_{c,\mathbf{q}}^{\nu\nu'}$ originates thus entirely from the *bubble*-term $\chi_{\mathbf{q}}^{0}(\nu)$.

Eq. (3.7) can be interpreted as a matrix equation summed over Matsubara frequencies. By multiplying the expression with the matrix inverse $[\chi_{c,\mathbf{q}}^{\nu\nu'}]^{-1}$ and $\left(\chi_{\mathbf{q}}^{0}(\nu)\right)^{-1}\delta_{\nu\nu'}$, we can solve Eq. (3.7) for $\chi_{c,\mathbf{q}}^{\nu\nu'}$ and obtain

$$\chi_{c,\mathbf{q}}^{\nu\nu'} = \left[\Gamma_c^{\nu\nu'} + (\chi_{\mathbf{q}}^{0})^{-1}\,\delta_{\nu\nu'}\right]^{-1}, \tag{3.8}$$

which we will refer to as the BSE of the *uniform* charge susceptibility. We recall that in DMFT only the local part of $\Gamma_c^{\nu\nu'}$ survives in the BSE, and thus can be can be extracted from the impurities as:

$$\Gamma_c^{\nu\nu'} = [\chi_{c,loc}^{\nu\nu'}]^{-1} - (\chi_{loc}^{0})^{-1}\delta_{\nu\nu'}, \tag{3.9}$$

with the *bubble*-term coefficient $\chi_{loc}^{0}(\nu) = -\beta G_{loc}(\nu)G_{loc}(\nu)$ and the generalized charge susceptibility $\chi_{c,loc}^{\nu\nu'} = \chi_{ph,\uparrow\uparrow,loc}^{\nu\nu'} + \chi_{ph,\uparrow\downarrow,loc}^{\nu\nu'}$:

$$\begin{aligned}\chi_{ph,\sigma\sigma',loc}^{\nu\nu'\omega} = &\int_0^\beta \mathrm{d}\tau_1\mathrm{d}\tau_2\mathrm{d}\tau_3\ \mathrm{e}^{-\mathrm{i}\nu\tau_1}\mathrm{e}^{\mathrm{i}(\nu+\omega)\tau_2}\mathrm{e}^{-\mathrm{i}(\nu'+\omega)\tau_3}\\ &\times\big\{\,\langle\mathcal{T}\hat{c}_{0\sigma}^{\dagger}(\tau_1)\hat{c}_{0\sigma}(\tau_2)\hat{c}_{0\sigma'}^{\dagger}(\tau_3)\hat{c}_{0\sigma'}(0)\rangle\\ &-\langle\mathcal{T}\hat{c}_{0\sigma}^{\dagger}(\tau_1)\hat{c}_{0\sigma}(\tau_2)\rangle\,\langle\mathcal{T}\hat{c}_{0\sigma'}^{\dagger}(\tau_3)\hat{c}_{0\sigma'}(0)\rangle\,\big\}.\end{aligned} \tag{3.10}$$

which are the output of the impurity solver, after the DMFT self-consistency is reached. Therefore, in DMFT the uniform generalized susceptibility $\chi_{c,\mathbf{q}}^{\nu\nu'}$ can be expressed in terms of the local charge susceptibility $\chi_{c,loc}^{\nu\nu'}$ by

$$\chi_{c,\mathbf{q}}^{\nu\nu'} = \left[[\chi_{c,loc}^{\nu\nu'}]^{-1} + \big((\chi_{\mathbf{q}}^{0})^{-1} - (\chi_{loc}^{0})^{-1}\big)\delta_{\nu\nu'}\right]^{-1}. \tag{3.11}$$

Whenever DMFT is used as an approximation for finite dimensional systems, several sum rules for the physical susceptibilities (e.g, those related to the Pauli-principle) are violated [21]. For example $\sum_{\mathbf{q}}\chi_{\mathbf{q}}^{c} \neq \chi_{loc}^{c}$, with $\chi_{\mathbf{q}}^{c} = \frac{2}{\beta^2}\sum_{\nu\nu'}\chi_{c,\mathbf{q}}^{\nu\nu'}$ and $\chi_{loc}^{c} = \frac{2}{\beta^2}\sum_{\nu\nu'}\chi_{c,loc}^{\nu\nu'}$. If one wants to overcome this problem one may perform a Moriyasque λ correction [41, 42]. This correction accounts for the overestimated correlation length ξ in DMFT of the Ornstein-Zernike function in Eq. (3.3). Thereby, one applies the transformation

$$(\chi_{\mathbf{q}}^{c}(\omega))^{-1} \to (\chi_{\mathbf{q}}^{c}(\omega))^{-1} + \lambda \tag{3.12}$$

in such a way that the sum rules are fulfilled. However, we are not interested in this aspect here.

On the other hand, although several sum rules are violated, DMFT is still a *conserving* theory at the 2P-level, i.e. the self-energy Σ and the irreducible vertex Γ_c can be both derived as functional derivative of a generating functional $\Phi[G_{loc}]$ (the Luttinger-Ward functional), by $\Sigma = \delta\Phi[G_{loc}]/\delta G_{loc}$ and $\Gamma_c = \delta\Sigma[G_{loc}]/\delta G_{loc}$ [4, 13, 17] which corresponds to the DMFT self-consistency. This guarantees that the condition of Eq.(3.2) – $\chi_{\mathbf{q}}^{c} = \partial n/\partial\mu$ – for the uniform susceptibility holds in DMFT [43].

3.4 Vertex Divergences

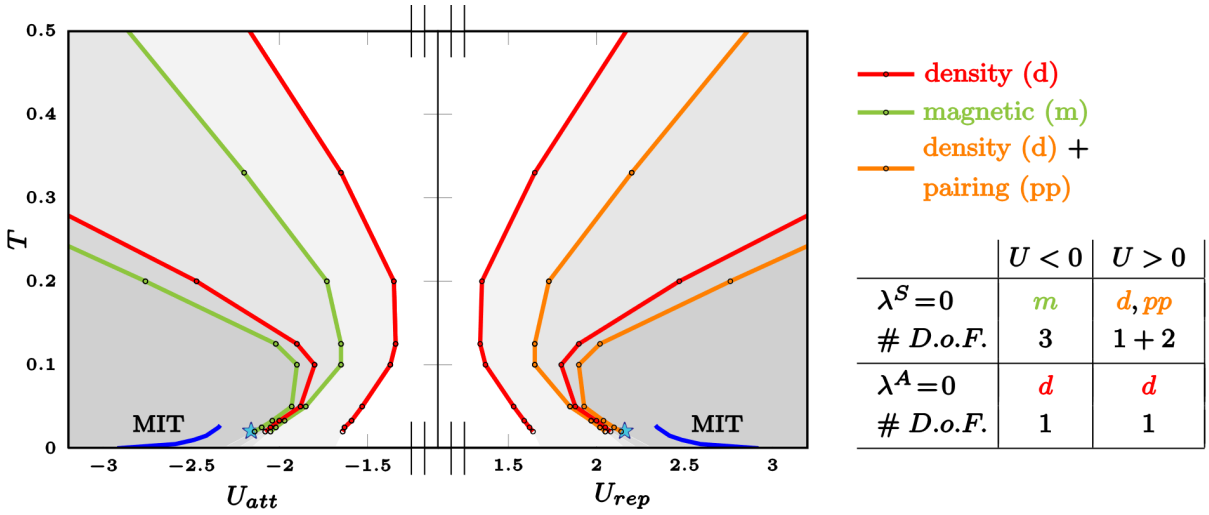

	$U<0$	$U>0$
$\lambda^S=0$	m	d, pp
# D.o.F.	3	1 + 2
$\lambda^A=0$	d	d
# D.o.F.	1	1

FIG. 3.2: Divergence lines of Γ_r in the $U-T$ phase diagram of the attractive (negative x-axis) and repulsive (positive x-axis) Hubbard model at half-filling ($n=1$, $\mu=U/2$). Red lines denote divergence lines in the charge channel (here denoted as density), green lines in the spin channel (denoted as magnetic), and orange lines both in the charge (density) and particle particle (pairing) channel. The table on the lower right compares the degrees of freedom (D.o.F.) of the corresponding channels and the symmetry (symmetric/anti-symmetric: λ^S/λ^A) of the associated eigenvectors of $\lambda=0$ of $\chi^{\nu\nu'}_{r,loc}$ at the divergence line. The figure has been taken from Ref. [11].

Taking a quick glance at Eq. (3.9):

$$\Gamma_c^{\nu\nu'} = [\chi_{c,loc}^{\nu\nu'}]^{-1} - (\chi^0_{loc})^{-1}\delta_{\nu\nu'}$$

we notice that whenever $\chi^{\nu\nu'}_{c,loc}$ has an eigenvalue $\lambda=0$, becomes a singular matrix, making $\Gamma_c^{\nu\nu'}$ divergent.

The divergence of the local irreducible 2P vertex $\Gamma_r^{\nu\nu'}$ in different channels r has been found in all fundamental many-body models [7–11], along several lines (divergence lines, in fact infinitely many) in the corresponding phase diagrams (see Fig. 3.2 for the Hubbard model). Somewhat surprisingly, they are already present in the metallic Fermi-liquid regime (where the 1P irreducible vertex – i.e. the self-energy Σ – is still Taylor expandable at low frequencies). These vertex divergences have severe impact on the cutting edge many-body algorithms, such as extensions of DMFT to the non-local case (DΓA, QUADRILEX) [6], Bold Diagrammatical Monte Carlo [12, 13, 44], and Nested Cluster Schemes [9].

What happens is the following: the eigenvalues λ of $\chi^{\nu\nu'}_{r,loc}$ – associated to the divergence of $\Gamma_r^{\nu\nu'}$ – have been observed to become negative after crossing zero. At half-filling, this trend has been related to the suppression of the associated physical susceptibility [11, 13]: for the repulsive Hubbard model a higher repulsion U will lead to a local moment formation, thus, to a suppression of the local charge response (χ^c_{loc}). At intermediate U, increasing the repulsion will lower positive eigenvalues of the generalized susceptibility, however for larger U – in the strongly interacting regime – the suppression is mostly made by the contribution of the negative eigenvalues λ of $\chi^{\nu\nu'}_{c,loc}$ appearing after the divergence lines.

In this respect, we note that at half-filling, $\chi^{\nu\nu'}_{r,loc}$ ($r=c,s$) is a centrosymmetric

matrix[5], due to the particle-hole symmetry of the model (see Tab. 2.1 by combining it with complex conjugation) [11], which leads to either completely symmetric or antisymmetric eigenvectors ($\mathbf{v}(\nu) = \mathbf{v}(-\nu)$ or $\mathbf{v}(\nu) = -\mathbf{v}(-\nu)$) of $\chi^{\nu\nu'}_{r,loc}$. In the calculation of the physical susceptibility $\chi^{r}_{loc} = \frac{2}{\beta^2}\sum_{\nu\nu'}\chi^{\nu\nu'}_{r,loc}$ the eigenvalues corresponding to the antisymmetric eigenvectors λ^A, yield no contribution since $[\sum_{\nu'}\mathbf{v}^{-1}(\nu')] \times [\sum_{\nu'}\mathbf{v}(\nu)] = 0$. Therefore, only the eigenvalues λ^S of the symmetric eigenvectors lead to the physical suppression of the susceptibility. This peculiar property has striking consequences for the divergence lines: By performing a pseudo-spin to spin transformation: $\hat{c}_{i\uparrow} \to \hat{c}_{i\uparrow}$ and $\hat{c}_{i\downarrow} \to (-1)^{-1}\hat{c}^{\dagger}_{i\downarrow}$, with i being the index of the lattice site, the repulsive Hubbard model can be mapped to the attractive Hubbard model $U \to -U$ at half-filling.

For the attractive Hubbard model, the local moment gets gradually suppressed by increasing interaction strength U, and hence also the local spin susceptibility χ^{s}_{loc} does so. One thus, expects and does actually observe a mapping of the divergence lines of the charge channel to the spin channel (orange to green lines in Fig. 3.2). This is however only true for the divergence lines of λ^S. The divergence lines of λ^A (red lines) are instead completely mirrored and appear for both cases in the charge channel, the supressing effect of the vertex divergences can be only associated with λ^S.

3.5 Proposed Connection

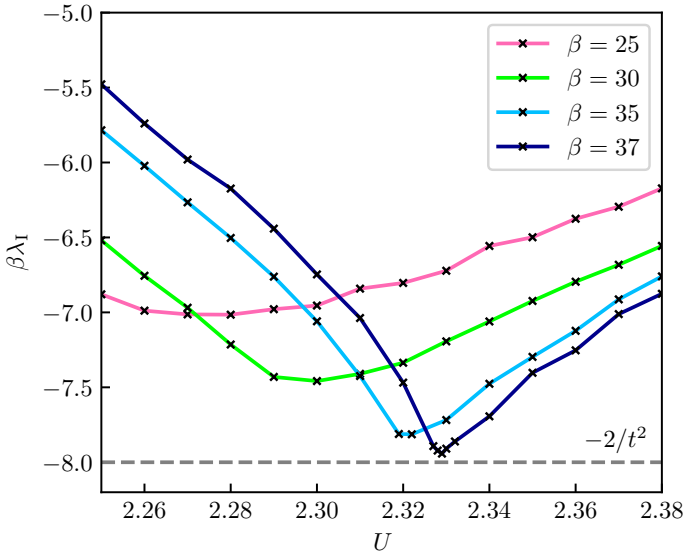

FIG. 3.3: Lowest eigenvalue λ (in this figure $2\lambda/\beta =: \beta\lambda_{\mathrm{I}}$) for different inverse temperatures $\beta = 1/T$ and U of the Hubbard model at half-filling for the Bethe lattice ($t = 1/2$). The dashed line indicates the proximity to the condition $\lambda = -\beta/t^2$ (here $\beta\lambda_{\mathrm{I}} = -2/t^2$). The figure has been taken from Ref. [28].

We already showed in Sec. 3.1 – by using the RPA – that he enhancement of the compressibility κ as well as the uniform charge susceptibility $\chi^{c}_{\mathbf{q}=\mathbf{0}}$ near the critical endpoint out of half-filling, can be interpreted as an effective attraction. In Ref. [15] it has been proposed that, indeed, a large negative irreducible vertex $\Gamma^{\nu\nu'}_{c}$ – which appears also right

[5]In fact, due to the additional time reversal symmetry (see Tab. 2.1) $\chi^{\nu\nu'}_{r,loc}$ is even a real *bisymmetric* matrix at half-filling and has therefore only real eigenvalues.

after a divergence line – might be responsible for this phenomena. However, then important questions remain: why not such an enhancement is observed after each divergence line, and how can this be connected to the previous understanding of the correspondence of the divergence lines with the suppression of the local susceptibility χ^c_{loc}.

In order to address these questions further, we express Eq. (3.11) in the spectral decomposition of the generalised susceptibility matrix

$$\chi^{\nu\nu'}_{c,loc} = \sum_j \lambda_j \mathbf{v}_j^{-1}(\nu') \otimes \mathbf{v}_j(\nu), \tag{3.13}$$

where λ_j are the eigenvalues and $\mathbf{v}_j(\nu)$ the eigenvectors of $\chi^{\nu\nu'}_{c,loc}$.

In the calculation of the physical susceptibility $\chi^c_{loc} = \frac{2}{\beta^2}\sum_{\nu\nu'}\chi^{\nu\nu'}_{c,loc}$ we then can express the sum over the eigenvectors as spectral weights $w_j = [\sum_{\nu'}\mathbf{v}_j^{-1}(\nu')] \times [\sum_{\nu}\mathbf{v}_j(\nu)]$. For the Bethe lattice[6] in the limit of infinite connectivity, it can be shown [4] that $(\chi^0_{\mathbf{q}=\mathbf{0}})^{-1} - (\chi^0_{loc})^{-1}$ is equivalent to the constant t^2/β independent of the filling n, and hence we end up with the expression

$$\chi^c_{\mathbf{q}=\mathbf{0}} = \frac{2}{\beta^2}\sum_j \left(\frac{1}{\lambda_j} + t^2/\beta\right)^{-1} w_j, \tag{3.14}$$

this means that $\chi^c_{\mathbf{q}=\mathbf{0}} \to \infty$ if $\lambda_j \to -\beta/t^2$, but *only* if $w_j \neq 0$

In such case, a strong dichotomy in the behaviour of χ^c_{loc} and $\chi^c_{\mathbf{q}=\mathbf{0}]}$ in the proximity of this condition must be expected. Computations for the Bethe lattice at half-filling, with $t = 1/2$, show (Fig. 3.3) that only the lowest eigenvalue, corresponding to an antisymmetric eigenvector and thus zero weight meets this condition. Remarkably, the DMFT results also demonstrate that this precisely happens at the critical endpoint of the MIT. The centrosymmetry of $\chi^{\nu\nu'}_{c,loc}$ explains, why $\chi^c_{\mathbf{q}=\mathbf{0}}$ is neither enhanced and (of course) nor divergent at half-filling.

In order to investigate this further, we aim to extend our study *out* of half-filling, where the matrix is no longer centrosymmetric and the strict condition of either symmetric or antisymmetric eigenvectors does not apply. For this study, we chose a more realistic ($2d$-square) lattice although Eq. (3.14) is then no longer rigorously valid, this will allow for a momentum resolved analysis. The results which represent the main original findings of the Master thesis are presented in the next chapter.

[6]The Bethe lattice has the following definition: every lattice site has the same number of neighbours (connectivity), thereby no closed loops can be obtained.

Chapter 4

Results and Discussion

"Wer sich Ziele setzt, geht am Zufall vorbei."
-Stefan Zweig

After discussing in chapter 3.5 the general idea, and the open questions regarding the connection of vertex divergences and the increase of the compressibility κ, we present here our numerical results. In particular two regions of the phase-space of the one-band Hubbard model on a square-lattice ($t = 1/4$) are analysed by means of DMFT, in close proximity of the Mott MIT. Thereby, we first take a cut in parameter space very close to the critical end point of the MIT at half-filling, interaction strength $U = 2.4$, and relatively high T ($T = 1/50,\ 1/53$). An additional region of interest – where the phase-separation instability is slightly more far away from half-filling at $U = 2.8$ and lower T ($T = 1/120$) – will be discussed in the second section. Calculations in the latter regime present increased numerical difficulties, which will be explicitly discussed. Both regions of interest are marked in Fig. 3.1 by green arrows. The DMFT calculations were performed with the w2dynamics *package [26].*

4.1 U = 2.4

For the analysis of Eq. (3.14) we aim at calculating χ^c_{loc} and $\chi^c_{\mathbf{q}=\mathbf{0}}$ via the generalised 2P quantities $\chi^{\nu\nu'}_{c,loc}$, $\chi^{\nu\nu'}_{c,\mathbf{q}=\mathbf{0}}$ out of half-filling right above T_c where the compressibility $\kappa = \frac{1}{n^2}\frac{\partial n}{\partial \mu}$ is enhanced or almost divergent and compare the different contributions of their respective eigenvalues λ_j. Since for $U = 2.4$, the critical endpoint of the phase-separation ($T_c,\ n_c,\ \mu_c$) should be relatively near at half filling ($n = 1, \mu = U/2 = 1.2$) we expect to have the best chance, here, to relate the corresponding eigenvectors $\mathbf{v}_j(\nu)$ to the half-filling case, where they are well understood [11].

However, since the exact parameters of the critical endpoint are not well known for the square-lattice case, we first have to locate the region of interest by numerically less demanding computations. Therefore, we calculate the density n in respect to the chemical potential μ for various temperatures, the results are shown in Fig. 4.1. As already stated in Eq. (3.2), the derivative $\partial n/\partial \mu$ is equal to the charge susceptibility $\chi^c_{\mathbf{q}=\mathbf{0}}$.

In Fig. 4.1 at the high temperature $T = 1/\beta = 1/30$ we observe a monotonic decrease of $\partial n/\partial \mu$ towards half-filling ($n = 1,\ \mu = U/2 = 1.2$). At lower μ ($\mu \simeq 1.0$) the rather linear dependence of n and, thus, constant slope is typical for the more metallic regime, whereas the plateau behaviour around $n \approx 1$ with an approximately zero slope near half-filling ($\mu \simeq 1.175$) indicates a strong suppression of the electron mobility, i.e. s bad metallic, almost insulating behaviour. By lowering T we observe a decrease of n in the

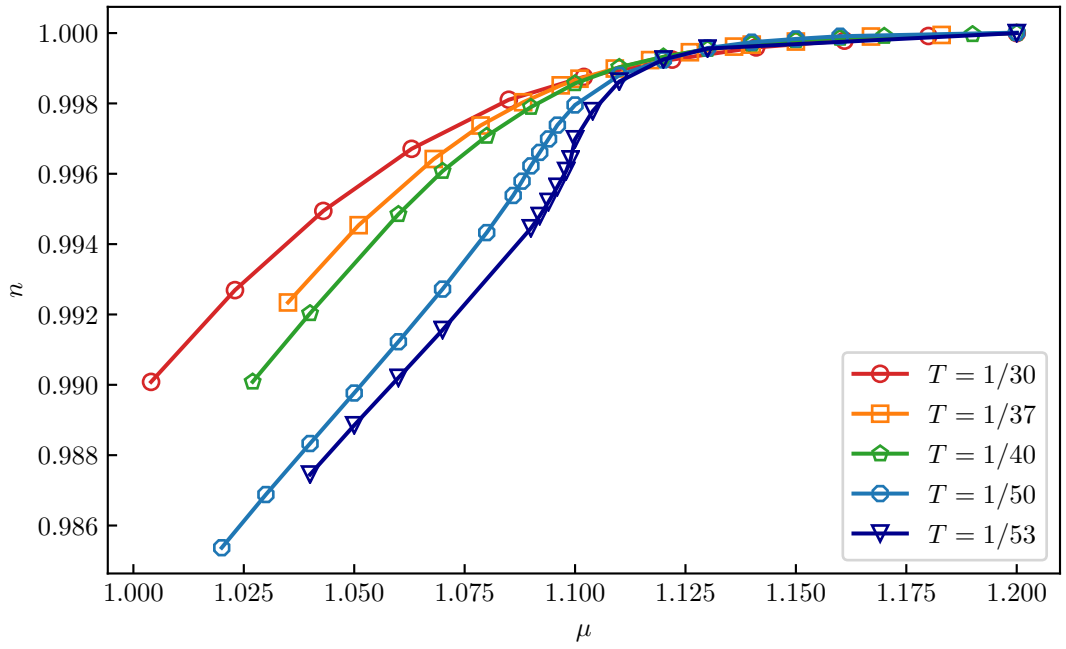

FIG. 4.1: Density n as a function of the chemical potential μ for $U = 2.4$ at different temperatures T computed in DMFT, by using *w2dynamics*. The data for $T = 1/53$ has been calculated by P. Chalupa.

metallic regime in contrast to the bad-metal near half-filling, where n is hardly changed. This difference in the behaviour of the two regimes eventually leads to an increase of the slope ($T = 50,\ 53$) in the middle at $\mu \simeq 1.09$ until the coexistence region is reached and the line gets discontinuous (diverging $\kappa \propto \partial n/\partial\mu$, not shown here).

Using the data shown in Fig. 4.1 the charge compressibility $\kappa = \frac{1}{n^2}\frac{\partial n}{\partial \mu}$ was calculated as the numerical derivative (described in 6.3 in the appendix). In Fig. 4.2a $\kappa(\mu)$ is displayed: for high-$T = 1/30$ the previously mentioned monotonic decrease of the compressibility is clearly visible. For $T = 1/53$, being just slightly above the critical endpoint T_c, a sharp maximum of κ is visible around $\mu = 1.1$, having an approximately three times higher value than for $\mu = 1.05$. Already at $\mu = 1.11$, κ rapidly decreases against half-filling at $\mu = 1.2$. By decreasing the temperature further, we expect the divergence of κ exactly at the critical endpoint at T_c.

Fig. 4.2b shows $\kappa(n)$, here we see how close to half-filling $n = 1$ this enhancement takes place. In addition the maximum appears to be nearly at the same values of $n \simeq 0.997$ for $T = 1/50,\ 1/53$.

In the following we focus on $T = 1/50$ and calculate $\chi^c_{\mathbf{q}=\mathbf{0}} = \frac{2}{\beta^2}\sum_{\nu\nu'}\chi^{\nu\nu'}_{c,\mathbf{q}=\mathbf{0}}$ for five different μ: (i) in the more metallic regime at $\mu = 1.105$, (ii) at the maximum of κ at $\mu = 1.088$, (iii) right after the maximum towards half-filling at $\mu = 1.1$, (iv) in the bad-metal phase at $\mu = 1.15$ and (v) exactly at half-filling at $\mu = 1.2$. In Fig. 4.3 the calculated $\chi^c_{\mathbf{q}=\mathbf{0}}$ is shown for those data points (red squares) and compared with the numerical derivative $\partial n/\partial\mu$ (blue circles), which should formally coincide [43]. The minor differences observed, can be explained by the numerical of the Monte Carlo data and the approximated high frequency dependence of $\chi^{\nu\nu'}_{c,\mathbf{q}=\mathbf{0}}$[1]. In addition Fig. 4.3 also compares the uniform $\chi^c_{\mathbf{q}=\mathbf{0}}$ with the local χ^c_{loc} charge susceptibility (grey pentagons) directly calcu-

[1]The high frequency asymptotic of $\chi^{\nu\nu'}_{c,\mathbf{q}=\mathbf{0}}$ in the calculation of $\chi^c_{\mathbf{q}=\mathbf{0}}$ was accounted for as summarized in the appendix, see Sec. 6.5.

(a)

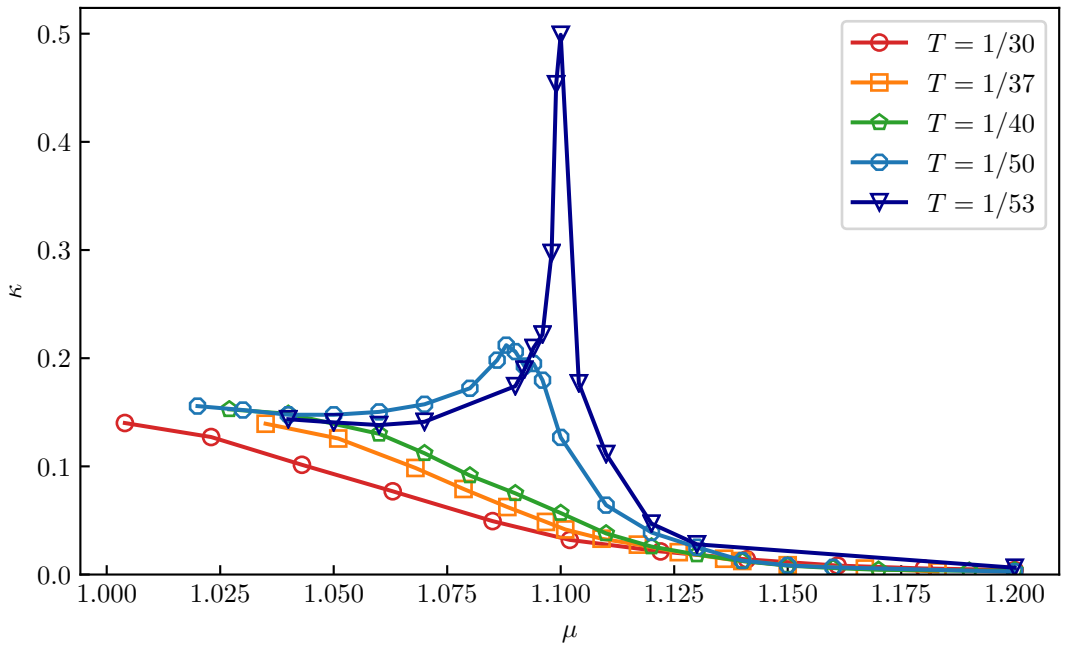

(b)

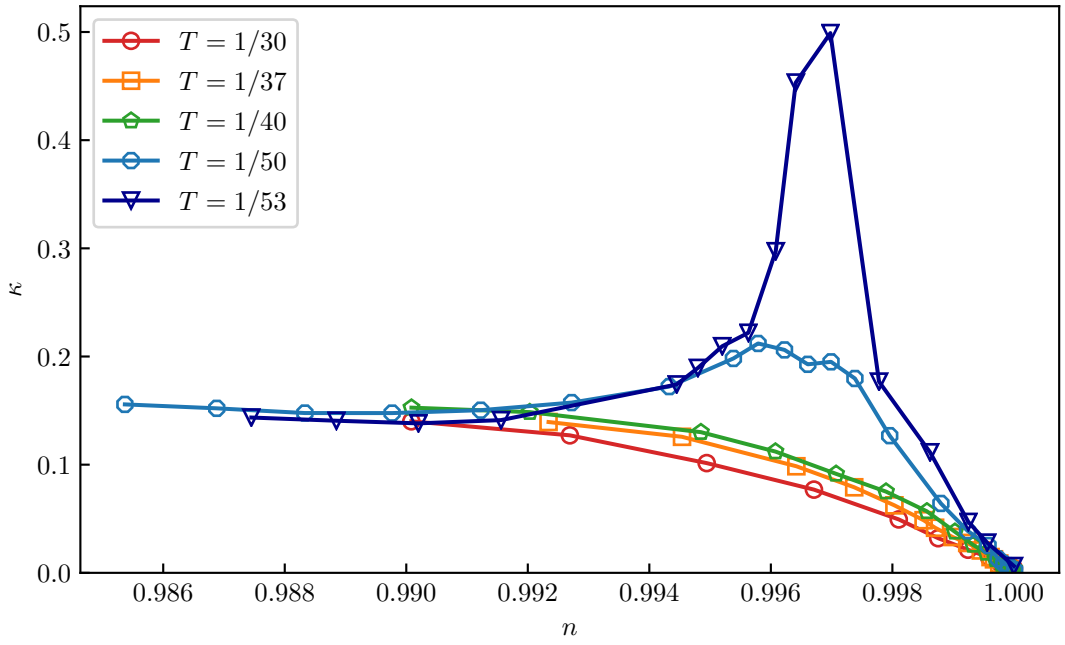

FIG. 4.2: Charge compressibility $\kappa = \frac{1}{n^2}\frac{\partial n}{\partial \mu}$ as function of the chemical potential μ (a) and as function of the density n (b) for $U = 2.4$ (in unit of $4t = 1$) at different temperatures T obtained from numeric derivation of the data in Fig. 4.1.

lated in *w2dynamics*. The *dichotomy* between the uniform and the local susceptibility is clearly visible: In χ^c_{loc} we see a monotonic suppression going towards half-filling, whereas $\chi^c_{\mathbf{q}=\mathbf{0}}$ is clearly enhanced around $\mu = 1.1$, and then quickly suppressed to nearly zero afterwards.

Both response functions can be calculated by Matsubara summation of the generalised susceptibilities $\chi^c_{loc} = \frac{2}{\beta^2}\sum_{\nu\nu'}\chi^{\nu\nu'}_{c,loc}$, $\chi^c_{\mathbf{q}=\mathbf{0}} = \frac{2}{\beta^2}\sum_{\nu\nu'}\chi^{\nu\nu'}_{c,\mathbf{q}=\mathbf{0}}$. In this respect, it is insightful to take a closer look at the lower Matsubara frequencies of those matrices, since they tend to give the larger contributions. Fig. 4.4 shows heat maps of $\chi^{\nu\nu'}_{c,loc}$ (bottom panels), $\chi^{\nu\nu'}_{c,\mathbf{q}=\mathbf{0}}$ (top panels): (i) before ($\mu = 1.05$, left panel), (ii) at ($\mu = 1.088$, middle panel), and (iii) right after the maximum ($\mu = 1.1$, right panel) of $\chi^c_{\mathbf{q}=\mathbf{0}}$. For $\chi^{\nu\nu'}_{c,loc}$ a dominant negative diagonal ($\nu = \nu'$ in blue) is seen, getting more and more negative towards half-filling. For $\chi^{\nu\nu'}_{c,\mathbf{q}=\mathbf{0}}$ the middle panel at $\mu = 1.088$ shows more intense colours at the maximum of $\chi^c_{\mathbf{q}=\mathbf{0}}$. Although negative and positive values in $\chi^{\nu\nu'}_{c,\mathbf{q}=\mathbf{0}}$ are significantly larger than for the local susceptibility, the slight asymmetry between diagonal and skew-diagonal entries – with the latter ones being larger than the former – accounts for the overall positive contribution of the inner Matsubara frequencies. This can be also observed by summing over larger and larger $2n \times 2n$ submatrices of $\chi^{\nu\nu'}_{c,\mathbf{q}=\mathbf{0}}$, where n is the maximal number of positive/negative Matsubara frequencies considered in the partial summation. For $\chi^{\nu\nu'}_{c,loc}$ the inner matrix elements give an net negative contribution to the sum and the overall positive value of the susceptibility is then guaranteed by the positive contributions of the high frequency asymptotic. On the contrary, $\chi^{\nu\nu'}_{c,\mathbf{q}=\mathbf{0}}$ shows a positive contribution in the inner part, which is then reduced by the intermediate frequency elements.

Further insight is obtained by the spectral decomposition of the generalised susceptibility matrices: $\chi^{\nu\nu'}$ ($\chi^{\nu\nu'}_{c,\mathbf{q}=\mathbf{0}}$ and $\chi^{\nu\nu'}_{c,loc}$) is diagonalized for the different parameter sets in the following way:

$$\sum_{\nu\nu'}\chi^{\nu\nu'} = \sum\nolimits_j \lambda_j \Big[\sum\nolimits_{\nu'} \mathbf{v}_j^{-1}(\nu')\Big] \times \Big[\sum\nolimits_{\nu} \mathbf{v}_j(\nu)\Big] = \sum\nolimits_j \lambda_j w_j. \tag{4.1}$$

The corresponding eigenvalues λ_j are shown in ascending order of $\mathrm{Re}\,\lambda_j$ in Fig. 4.5. In the top two panels the real (left) and imaginary part (right) of λ_j of $\chi^{\nu\nu'}_{c,\mathbf{q}=\mathbf{0}}$ are displayed, while in the bottom panels the eigenvalues of $\chi^{\nu\nu'}_{c,loc}$ are shown. Since $\chi^{\nu\nu'}$ is a centrohermitian matrix out of half-filling, its eigenvalues are either real $\lambda \in \mathbb{R}$ or complex conjugate pares $\lambda, \bar{\lambda} \in \mathbb{C}$ [45] (see Tab. 2.1 and appendix, Sec. 6.4). Interestingly, we always found at least two real eigenvalues. The two lowest real eigenvalues, with negative sign, are denoted by $\lambda_{\mathrm{I}} \coloneqq \lambda_\alpha$ and $\lambda_{\mathrm{II}} \coloneqq \lambda_\delta$ in the following. In the top left panel we see that $\lambda_\alpha = \lambda_{\mathrm{I}}$ gets extremely negative right at the maximum of $\chi^c_{\mathbf{q}=\mathbf{0}}$ at $\mu = 1.088$, whereas the other λ_j do not differ much from the eigenvalues of $\chi^{\nu\nu'}_{c,loc}$ [2].

This supports the original idea in Eq. (3.14): the most negative eigenvalue is negative enough to get close, or even to fulfil the condition β/t^2.

An objection to this interpretation, here, could be that this formula is valid for the Bethe lattice but not for the square-lattice used in our calculations. Nevertheless, we see that Eq. (3.14) holds approximately by defining an effective constant $t^2 \to t^2_{eff}$, thus providing a good key for the interpretation. In Fig. 4.6, the real (left panel) and imaginary part (right panel) of $t^2_{eff}/\beta \coloneqq (\chi^0_{\mathbf{q}=\mathbf{0}})^{-1} - (\chi^0_{loc})^{-1}$ as function of Matsubara frequencies is displayed. Although this term is no longer just a constant, it only shows small variations in ν for different μ at the lowest Matsubara frequencies in the real and imaginary part out of half-filling. We might also substitute the single valued condition β/t^2 with an effective

[2] Note that for half-filling all eigenvalues are real, since $\chi^{\nu\nu'}$ is centrosymmetric [11].

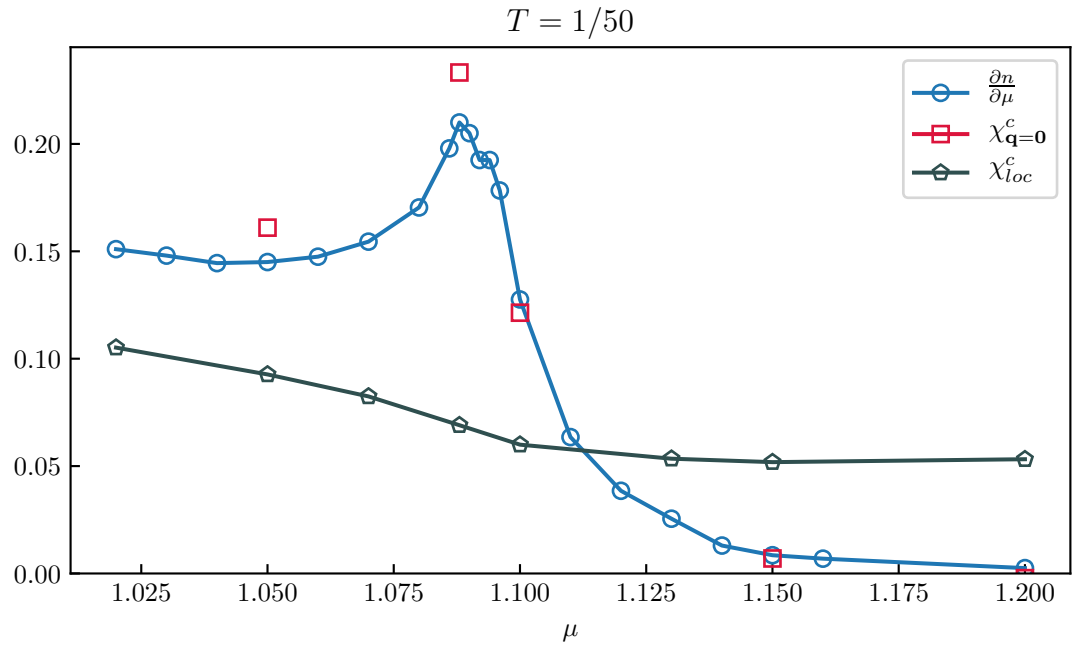

FIG. 4.3: Comparison between the numerical derivative $\partial n/\partial \mu$ and the static ($\omega = 0$) charge susceptibility $\chi^c_{\mathbf{q}=\mathbf{0}}$ in contrast to the static local charge susceptibility χ^c_{loc} of the auxiliary AIM as function of of the chemical potential μ for $U = 2.4$ and $T = 1/50$.

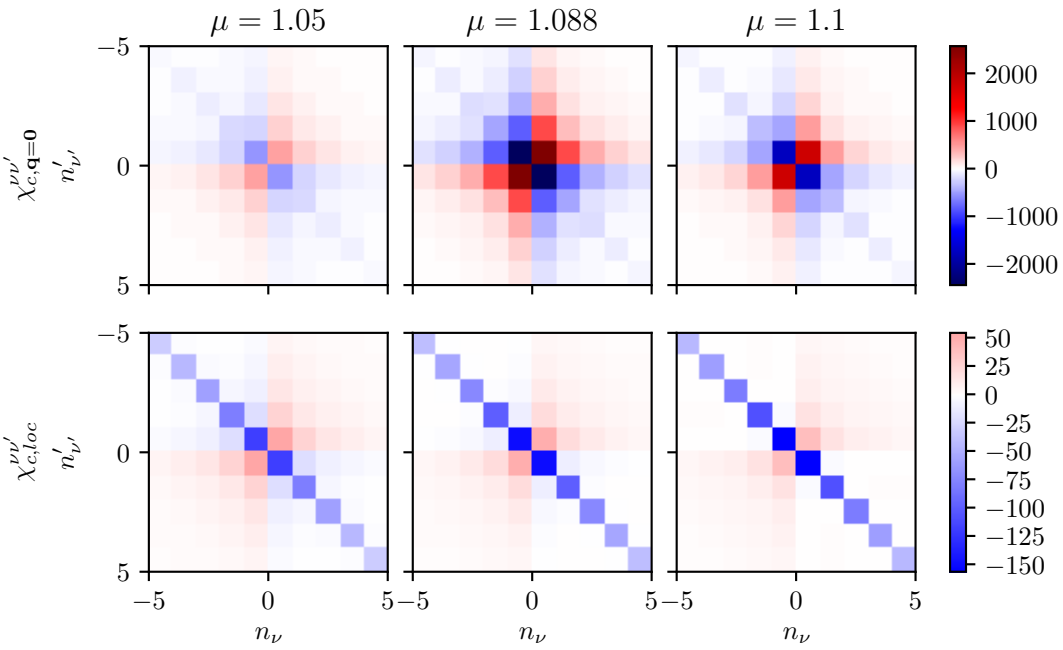

FIG. 4.4: Heat maps of the generalised charge compressibility $\chi^{\nu\nu'}_{c,\mathbf{q}=\mathbf{0}}$ and the generalised local charge susceptibility $\chi^{\nu\nu'}_{c,loc}$ of the auxiliary AIM as function of of the chemical potential μ for $U = 2.4$ and $T = 1/50$.

area β/t^2_{eff}, marking the overall variation in ν. We expect that the lowest eigenvalue λ_{I} will reach this effective area in the proximity of the critical endpoint T_c. This idea is displayed in Fig. 4.7. Indeed for $\mu = 1.088$ – at the maximum of $\chi^c_{\mathbf{q}=\mathbf{0}}$ – $\lambda_{\mathrm{I}}(\chi^c_{loc})$ (red line) *hits* this region of t_{eff} (blue area), however $\lambda_{\mathrm{II}}(\chi^c_{loc})$ (orange line) does not.

So far, these considerations do not explain *why* $\chi^c_{\mathbf{q}=\mathbf{0}}$ is *positively* enhanced since

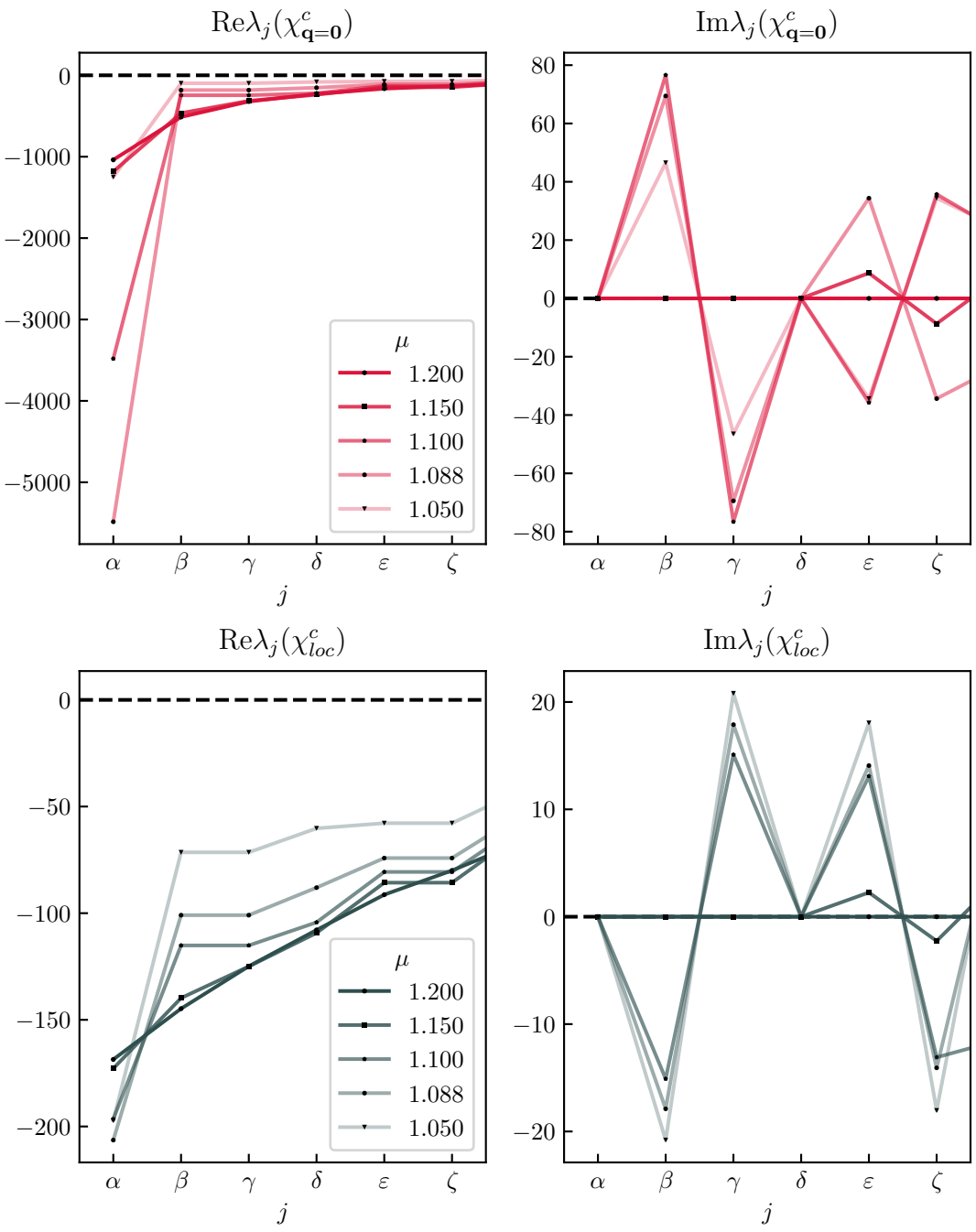

FIG. 4.5: Eigenvalues of the generalised uniform/local charge susceptibility $\chi^{\nu\nu'}_{c,\mathbf{q}=\mathbf{0}}/\chi^{\nu\nu'}_{c,loc}$ denoted by $\lambda_j(\chi^c_{\mathbf{q}=\mathbf{0}})$/ $\lambda_j(\chi^c_{loc})$ in the the top/bottom panels. Left: real part; right: imaginary part, for different chemical potentials μ ($\mu = 1.2$ – half-filling), at $U = 2.4$ and $T = 1/50$.

$\lambda_{\mathrm{I}}(\chi^c_{\mathbf{q}=\mathbf{0}})$ has a huge negative value. Fig. 4.8 resolves this: in the top panel λ_{I} (red) and λ_{II} (orange) of both $\chi^c_{\mathbf{q}=\mathbf{0}}$, χ^c_{loc}, and in the bottom panel the corresponding *weight* w_{I} (red) and w_{II} (orange) are shown. The key ingredient is the *negative* weight $w_{\mathrm{I}}(\chi^c_{\mathbf{q}=\mathbf{0}})$ of $\lambda_{\mathrm{I}}(\chi^c_{\mathbf{q}=\mathbf{0}})$ which can be seen in the bottom panel (red line). For both local and uniform $\chi^{\nu\nu'}$, w_{I} is negative out of half-filling, which is only possible because $\chi^{\nu\nu'}$ is no longer a hermitian matrix. Since the imaginary part of the corresponding physical susceptibilities χ^c has to be zero ($\chi^{\nu\nu'}$ is centrohermitian), the following condition has to be fulfilled:

$$\mathrm{Re}\left[\sum\nolimits_{\nu'} \mathbf{v}_j^{-1}(\nu')\right] \mathrm{Im}\left[\sum\nolimits_{\nu} \mathbf{v}_j(\nu)\right] = -\,\mathrm{Re}\left[\sum\nolimits_{\nu} \mathbf{v}_j(\nu)\right] \mathrm{Im}\left[\sum\nolimits_{\nu'} \mathbf{v}_j^{-1}(\nu')\right], \qquad (4.2)$$

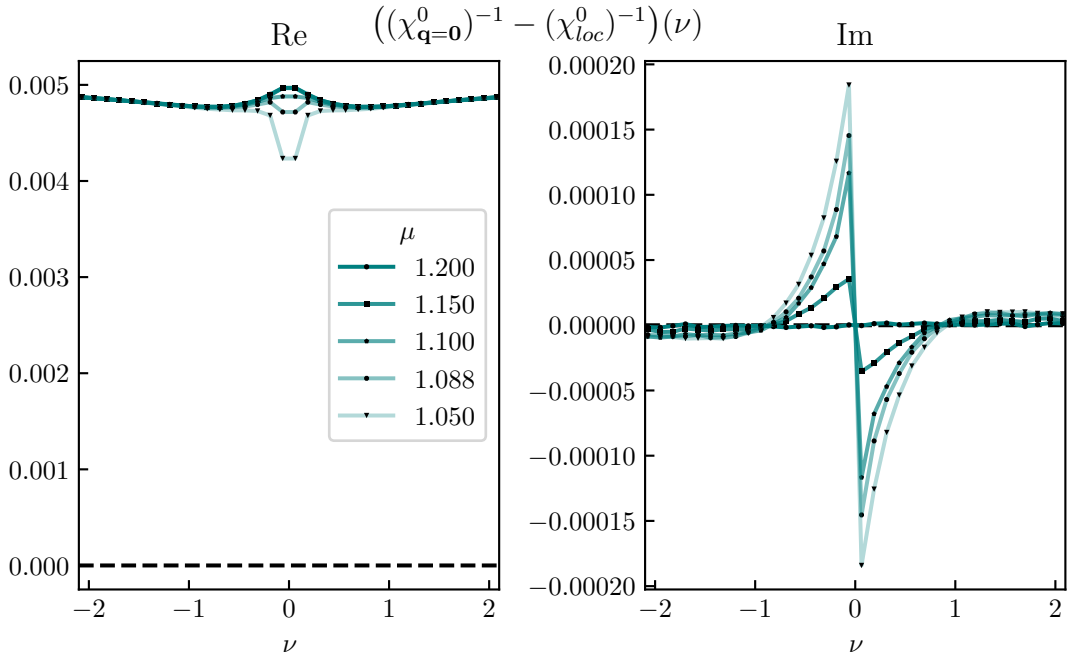

FIG. 4.6: Difference between the inverse of the uniform $\chi^0_{\mathbf{q}=\mathbf{0}}$ and local χ^0_{loc} *bubble* contribution of the generalised susceptibility. Left: real part; right: imaginary part, for different chemical potentials μ ($\mu = 1.2$ – half-filling), at $U = 2.4$ and $T = 1/50$.

and χ^c can only be negative if both summands in

$$w_j = \mathrm{Re}\left[\sum_{\nu'} \mathbf{v}_j^{-1}(\nu')\right] \mathrm{Re}\left[\sum_{\nu} \mathbf{v}_j(\nu)\right] - \mathrm{Im}\left[\sum_{\nu'} \mathbf{v}_j^{-1}(\nu')\right] \mathrm{Im}\left[\sum_{\nu} \mathbf{v}_j(\nu)\right] \tag{4.3}$$

yield negative contributions. However w_{II} still remains *positive*, and hence $\lambda_{\mathrm{II}} w_{\mathrm{II}} < 0$ contributes to a suppression of $\chi^c_{\mathbf{q}=\mathbf{0}}$.

$\lambda_{\mathrm{I}} w_{\mathrm{I}} > 0$, thus, explains the positive enhancement of $\chi^c_{\mathbf{q}=\mathbf{0}}$ created by a large negative $\lambda_{\mathrm{I}}(\chi^c_{\mathbf{q}=\mathbf{0}})$ in the vicinity of $\lambda_{\mathrm{I}}(\chi^c_{loc}) = -\beta/t^2_{eff}$. We note that the approximation of t^2_{eff} as a constant is further supported, a posteriori, by the almost identical weights of $\chi^{\nu\nu'}$ in the lower panel of Fig. 4.8.

We can substantiate further our analysis by analysing the different contributions in the overall sum of the physical susceptibility χ^c ($\chi^c_{\mathbf{q}=\mathbf{0}}$ and χ^c_{loc}) by splitting χ^c into the two contributions of the lowest two real eigenvalues and the rest:

$$\chi^c = \underbrace{\frac{2}{\beta^2}\lambda_{\mathrm{I}}\, w_{\mathrm{I}}}_{\mathrm{I}} + \underbrace{\frac{2}{\beta^2}\lambda_{\mathrm{II}}\, w_{\mathrm{II}}}_{\mathrm{II}} + rest. \tag{4.4}$$

We denote the first two contributions in the following simply by I and II. In Fig. 4.9 the results of this analysis is shown for five parameter sets, where the high frequency dependence of both χ^c has been approximated in the calculation. In the top/bottom panels the contributions of $\chi^c_{\mathbf{q}=\mathbf{0}}/\chi^c_{loc}$ are displayed. The major difference between the two stems from contribution I, which has a positive value and becomes largest at the maximum of $\chi^c_{\mathbf{q}=\mathbf{0}}$ at $\mu = 1.088$. II yielding a negative contribution, which is getting enhanced in $\chi^c_{\mathbf{q}=\mathbf{0}}$ for $\mu = 1.1$, but since the lowest complex conjugate pair $\lambda_\beta, \lambda_\gamma$ is getting also slightly increased the overall contribution of II and the *rest* does not change. Towards half-filling both contributions vanish.

Still, the question remains if the contributions I and II, stemming from the negative

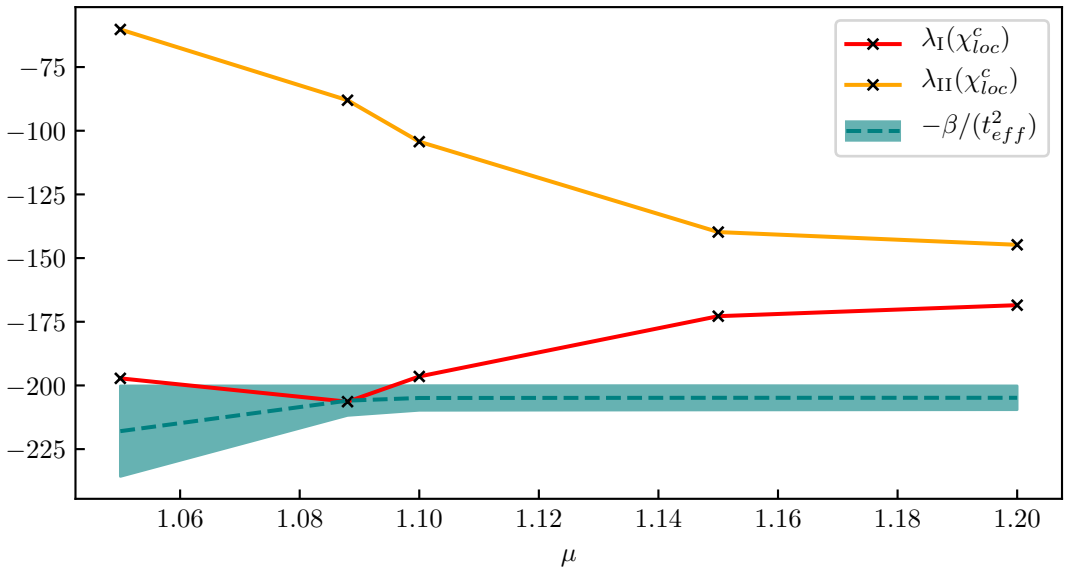

FIG. 4.7: Lowest real eigenvalues $\lambda_{\mathrm{I}}(\chi^c_{loc})$, $\lambda_{\mathrm{II}}(\chi^c_{loc})$ of the generalised local susceptibility $\chi^{\nu\nu'}_{c,loc}$ and the variation range of $\mathrm{Re}([\chi^0_{\mathbf{q}=\mathbf{0}}]^{-1} - [\chi^0_{loc}]^{-1})^{-1}$ over all Matsubara frequencies, denoted as $-\beta/t^2_{eff}$ in dependence of the chemical potential μ ($\mu = 1.2$ – half-filling), at $U = 2.4$ and $T = 1/50$.

real eigenvalues λ_{I}, λ_{II}, can be linked to the divergence lines at half-filling. As stated already in chapter 3.4 – at half-filling – two classes of eigenvalues λ_j are observed: (i) λ^S corresponding to symmetric eigenvectors ($\mathbf{v}_j(\nu) = \mathbf{v}_j(-\nu)$) and linked to supressing the physical susceptibility after the divergence of Γ and (ii) λ^A corresponding to anti-symmetric eigenvectors ($\mathbf{v}_j(\nu) = -\mathbf{v}_j(-\nu)$) which do not contribute because of their zero weight $w_j = 0$. In Fig. 4.10a the gradual development of $\mathbf{v}_{\mathrm{I}}(\nu)$ towards half-filling is displayed. At half-filling ($\mu = 1.2$), the eigenvector becomes real and perfectly anti-symmetric, out of half-filling the real part as a function of frequency remains rather similar, but is not strictly anti-symmetric anymore. For $\mathbf{v}_{\mathrm{II}}(\nu)$ in Fig. 4.10b a similar development is seen, but now towards a symmetric eigenvector at half-filling. Out of half-filling again an approximately symmetric shape in the real part persists.

We observe, again, that in this way, we can associate unambiguously the lowest real eigenvalue λ_{I}, leading to the increase in the compressibility κ, and ultimately to its divergence at the critical endpoint out of half-filling by fulfilling the condition $\lambda_{\mathrm{I}}(\chi^c_{loc}) = -\beta/t^2_{eff}$, to a red divergence line. The second lowest real eigenvalue λ_{II} is connected with an orange divergence line and is contributing to the suppression of χ^c_{loc} as well as κ.

We expect that for $T = 1/53$ where the maximum of κ is larger in value, λ_{I} will become more negative and contribution I will get more enhanced. Indeed, this can be observed in Fig. 4.11a and Fig. 4.11b. Fig. 4.11a compares –similar to Fig. 4.3 – $\partial n/\partial\mu$ with $\chi^c_{\mathbf{q}=\mathbf{0}}$ and χ^c_{loc} and Fig. 4.11b shows the different contributions I, II, and *rest* of χ^c for $T = 1/53$. Further calculations are planned for this parameter set.

4.1.1 q-Dependence of the charge susceptibility

It is insightful to compare $\chi^c_{\mathbf{q}}$ at the maximum of $\chi^c_{\mathbf{q}=\mathbf{0}}$ with the half-filling case and also determine the impact of contribution I, i.e. stemming from λ_{I}, onto the $\mathbf{q}$-dependent susceptibility. The results are displayed in Fig. 4.12. We see that the enhancement takes

place at $\mathbf{q} = \mathbf{0}$ only (top left), and that it stems entirely from I (bottom left). Without this contribution $\chi^c_{\mathbf{q}}$ at $\mu = 1.1$ (bottom right) shows a remarkable similarity with $\chi^c_{\mathbf{q}}$ at half-filling (top right). At half-filling a minimum at $\mathbf{q} = \mathbf{0}$ and a weak maximum at $\mathbf{q} = (\pi, \pi)^T$ is seen, where the asymmetric eigenvector results in a zero weight w_{I}. For an interpretation see Ref. [28]. At $\mathbf{q} = \mathbf{0}$ a fit to a Ornstein-Zernike function was made to extract the corresponding correlation length ξ. This is illustrated in Fig. 4.13a for $T = 1/50$. By going from $T = 1/50$ (orange) to $T = 1/53$ (green) ξ is increasing near the critical endpoint, as shown in Fig. 4.13b. At T_c $\xi \to \infty$, as expected due to the second-order phase transition nature of the critical endpoint(s).

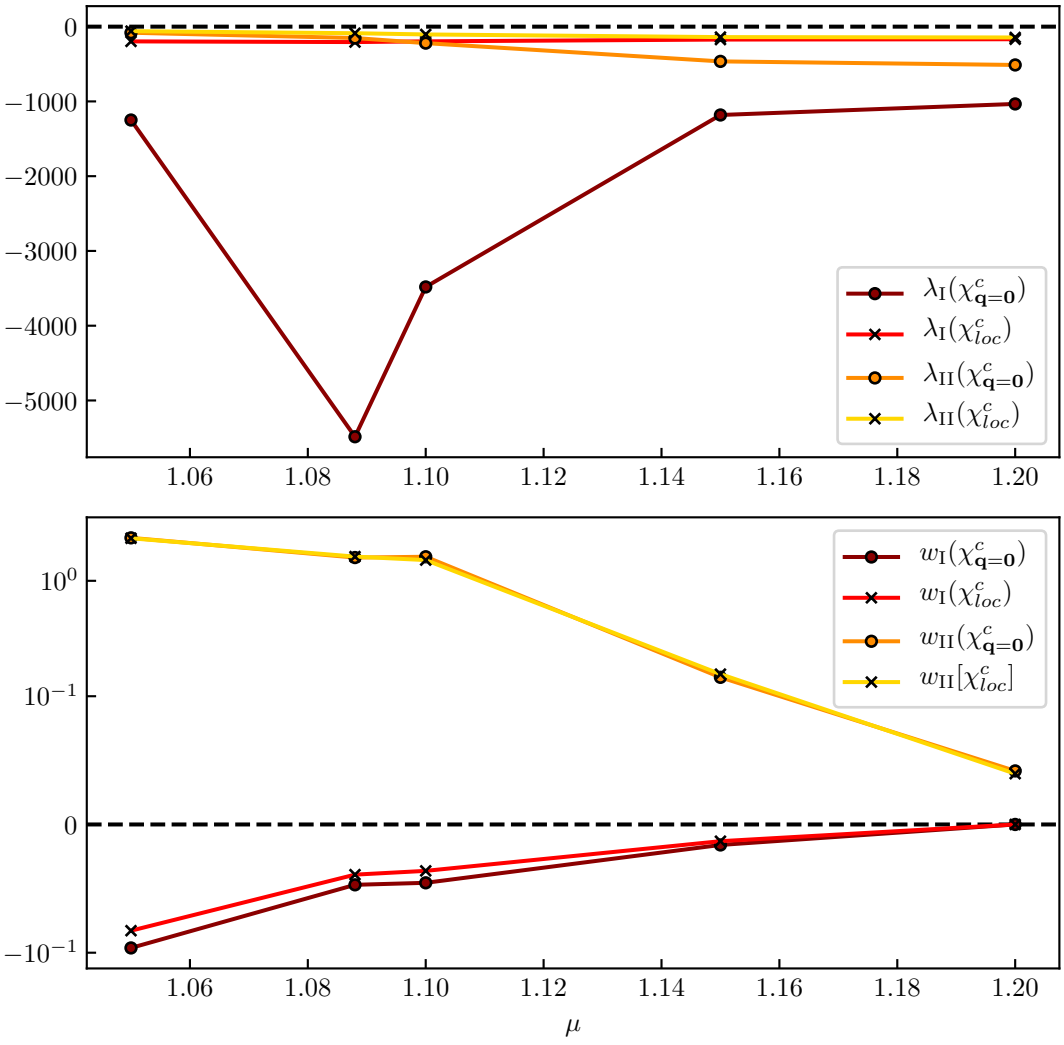

FIG. 4.8: Lowest two real eigenvalues/weights λ_{I}, $\lambda_{\mathrm{II}}/w_{\mathrm{I}}$, w_{II} of the uniform $\chi^c_{\mathbf{q}}$ and local χ^c_{loc} charge susceptibility in the top/bottom panel for different μ at $T = 1/50$, $U = 2.4$.

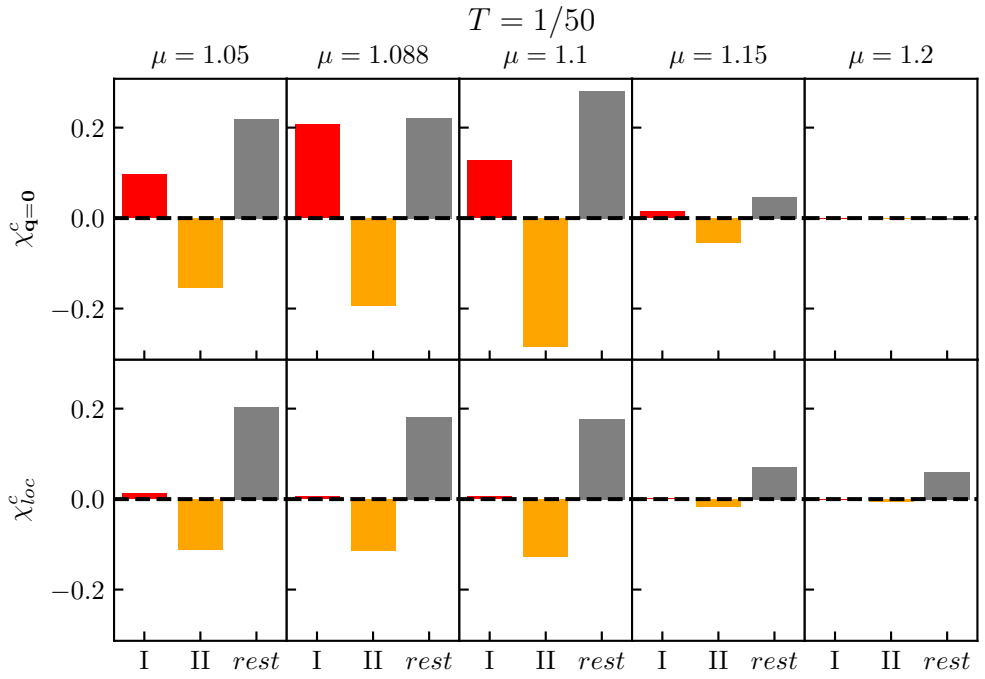

FIG. 4.9: Different contributions of $\chi^c = \mathrm{I} + \mathrm{II} + rest$ of the uniform $\chi^c_{\mathbf{q}}$ (upper panels) and local χ^c_{loc} (lower panels) charge susceptibility for different μ ($\mu = 1.2$ – half-filling) at $T = 1/50$, $U = 2.4$. The maximum of $\chi^c_{\mathbf{q}}$ is found at $\mu = 1.088$.

(a)

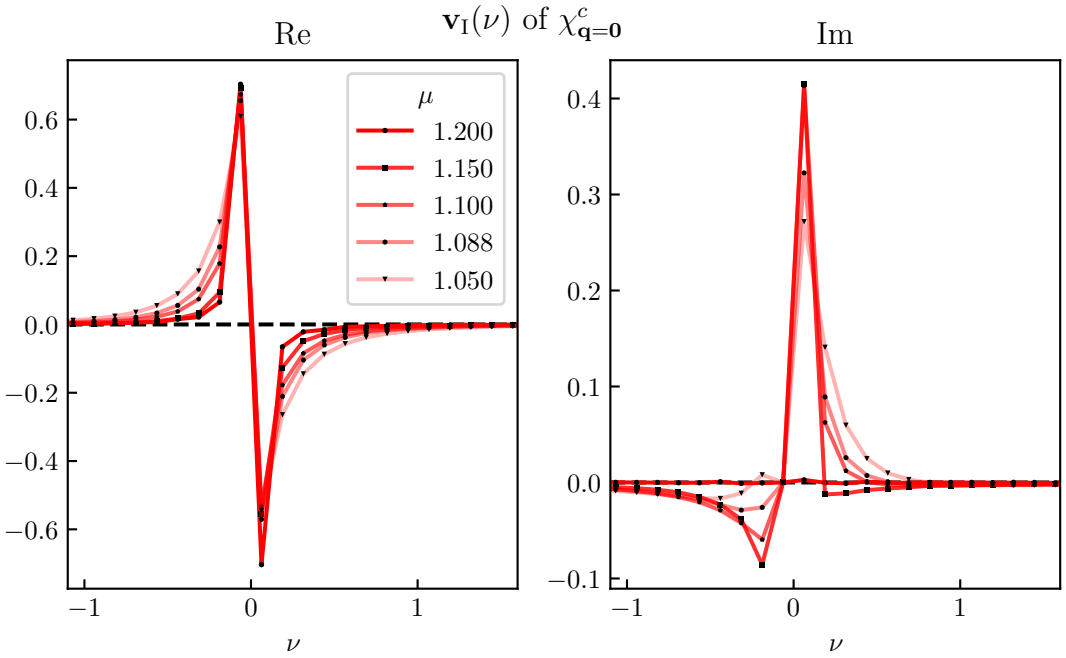

(b)

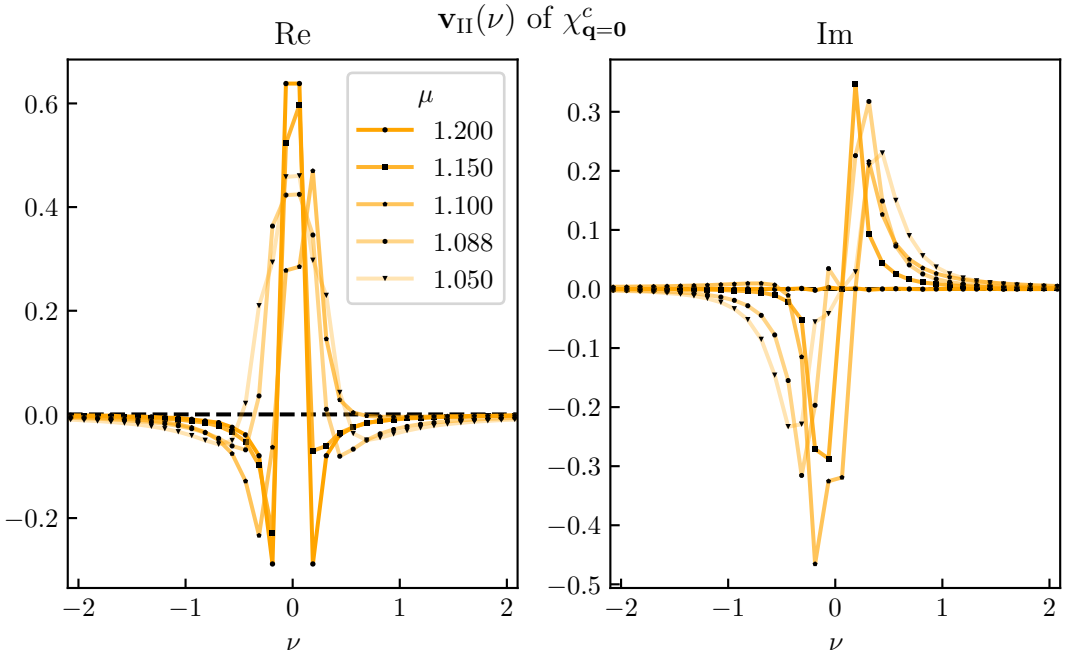

FIG. 4.10: Eigenvector $\mathbf{v}_{\mathrm{I}}(\nu)/\mathbf{v}_{\mathrm{II}}(\nu)$ of the first/second lowest real eigenvalue $\lambda_{\mathrm{I}}/\lambda_{\mathrm{II}}$ of the uniform susceptibility $\chi^{c}_{\mathbf{q}=\mathbf{0}}$ in (a)/(b) for different chemical potentials μ ($\mu = 1.2$ – half-filling). Left: real part; right: imaginary part, at $U = 2.4$ and $T = 1/50$.

(a)

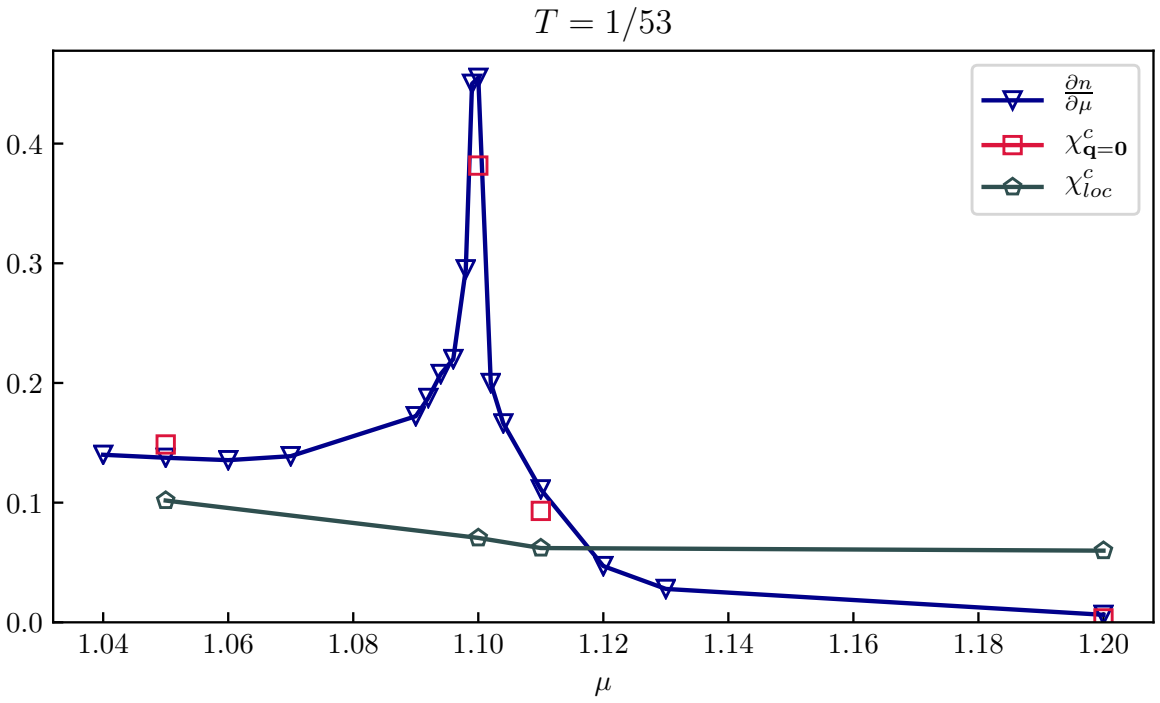

(b)

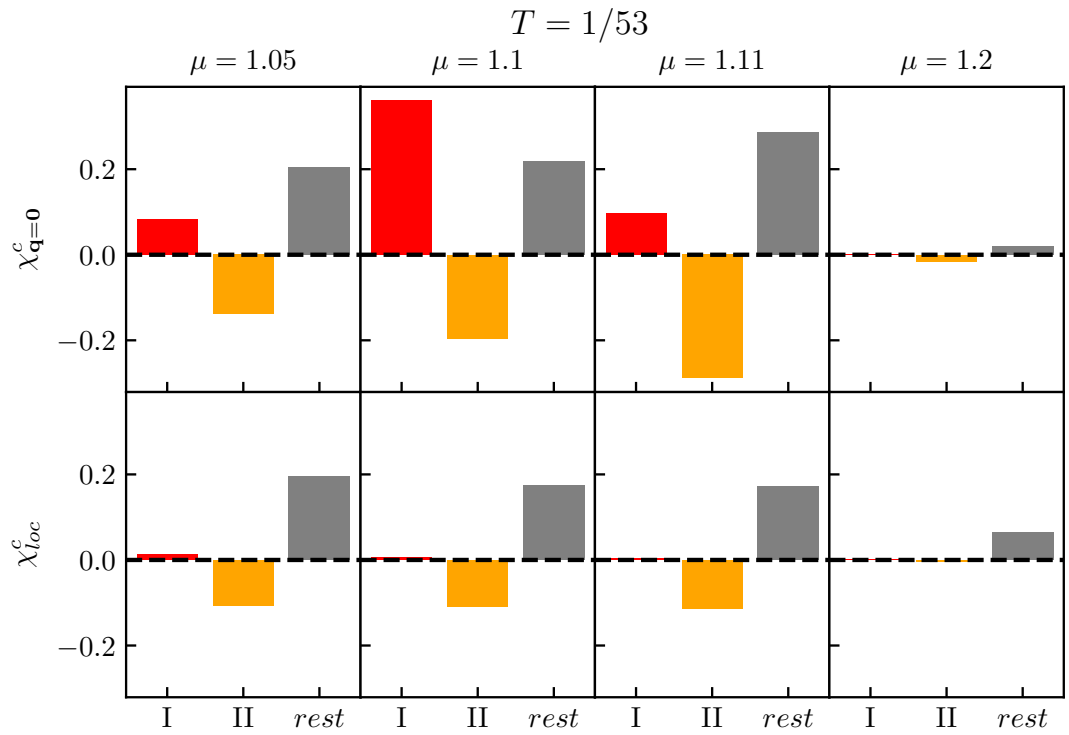

FIG. 4.11: (a): comparison of the numerical derivative $\partial n/\partial \mu$, the uniform charge susceptibility $\chi^c_{\mathbf{q}=\mathbf{0}}$, and the local charge susceptibility χ^c_{loc} for $T = 1/53$ and $U = 2.4$. (b): different contributions of $\chi^c = \mathrm{I} + \mathrm{II} + rest$ for different μ for the same T and U.

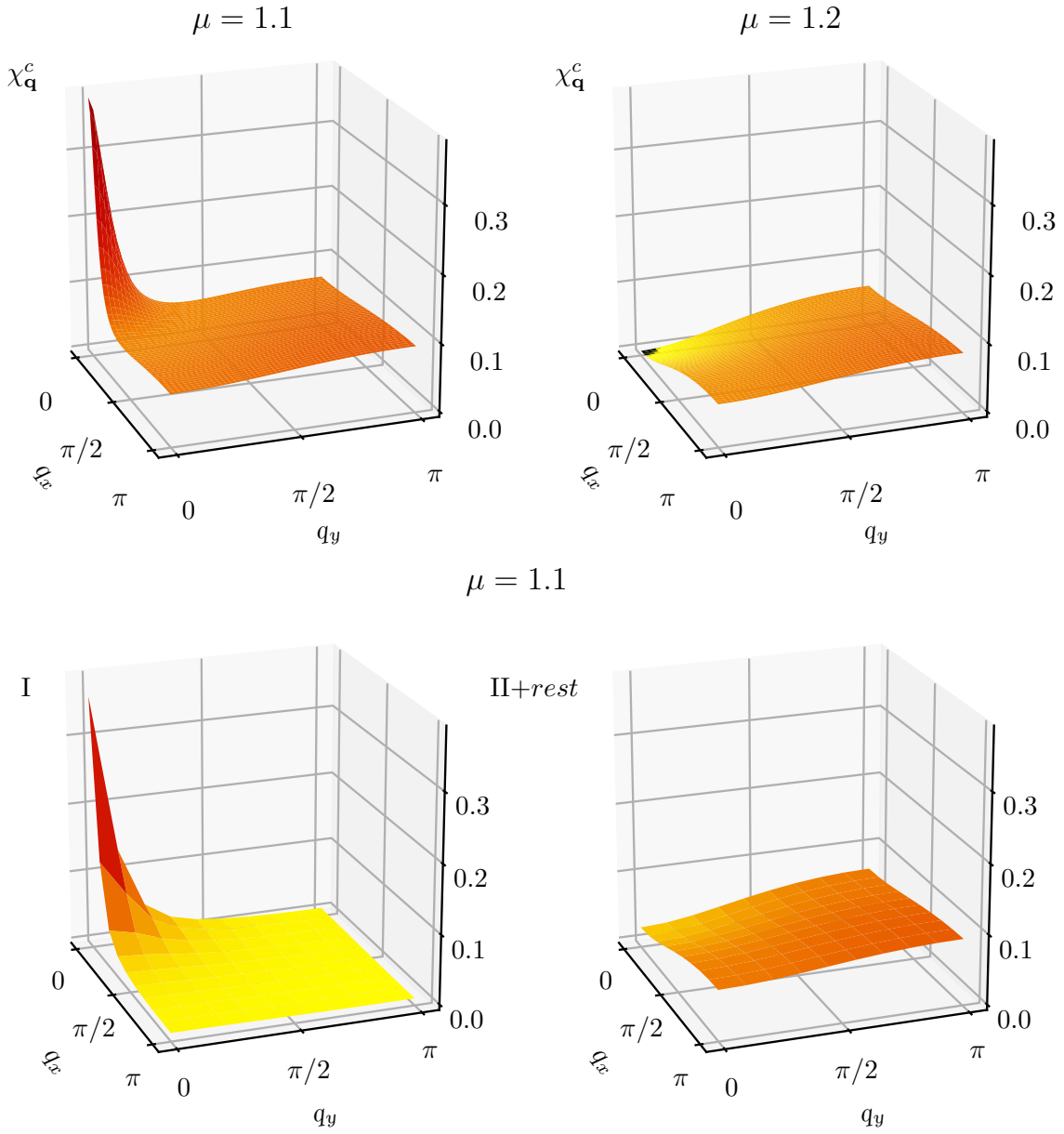

FIG. 4.12: Static ($\omega = 0$) charge susceptibility $\chi^c_{\mathbf{q}}$ for the local maximum of κ at $\mu = 1.1$ in the top left panel and for half filling at $\mu = U/2 = 1.2$ in the top right panel. Different contributions of $\chi^c_{\mathbf{q}} = \mathrm{I} + \mathrm{II} + \mathit{rest}$ depending on $\mathbf{q}$ in the bottom panels. Left: I; bottom right: $\mathrm{II} + \mathit{rest}$, for $U = 2.4$ and $T = 1/53$.

(a)

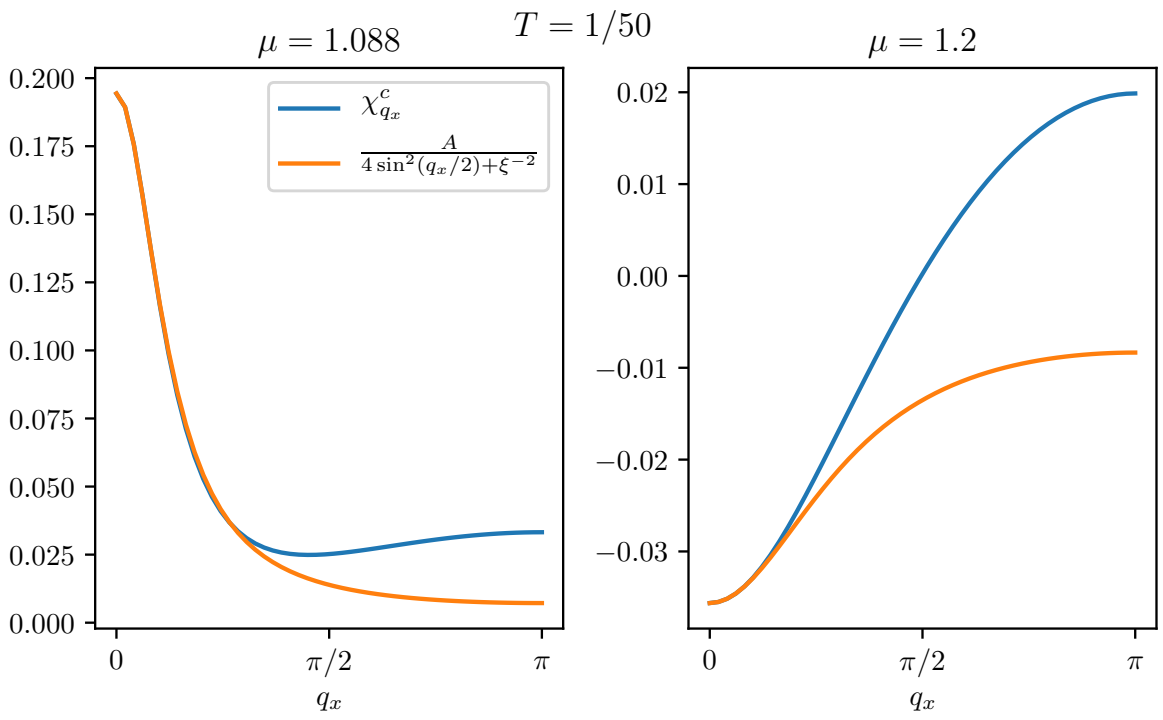

(b)

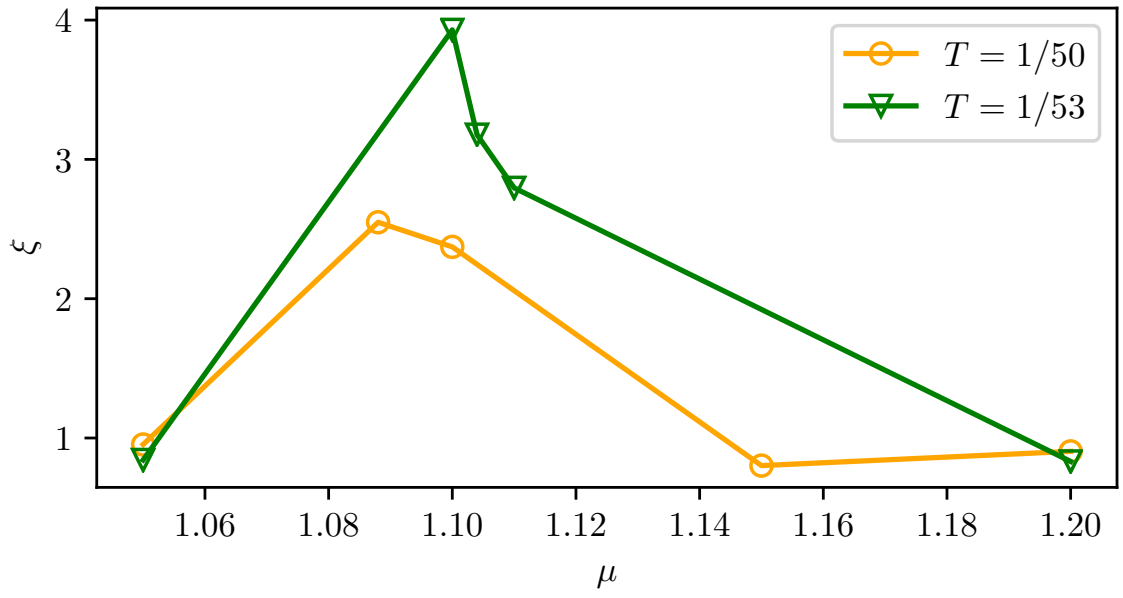

FIG. 4.13: (a): Fit of to the charge susceptibility $\chi^c_{q_x}$ (blue) using the Orstein-Zernike function (orange) for the local maximum of κ at $\mu = 1.088$ and for half filling at $\mu = U/2 = 1.2$ to extract the correlation length ξ. (b): correlation length ξ for $T = 1/50$ (orange) and $T = 1/53$ (green) as function of μ at $U = 2.4$.

4.2 U = 2.8

For $U = 2.8$ the critical endpoint of the phase-separation is found at lower T and at a slightly higher doping level (smaller n), as schematically illustrated in Fig. 3.1. This can be also seen in Fig. 4.14a, where the calculated numerical derivative $\partial n/\partial \mu$ as function of the chemical potential μ is shown (blue circles) for $T = 1/120$. The enhancement indicating the position of the critical endpoint lies further away from half-filling $\mu = U/2 = 1.4$ than for $U = 2.4$ in Fig. 4.3 though always within the small range of 1%. When performing the same decomposition of $\chi^c = \mathrm{I} + \mathrm{II} + rest$ as for $U = 2.4$ in Fig. 4.14b the qualitative outcome does not change: The dominating contribution in $\chi^c_{\mathbf{q}=\mathbf{0}}$ is found to be originated by λ_I and for $U = 2.8$ it is even more dominant.

However, in the bad-metal regime, already at $\mu = 1.07$, only complex-conjugate pairs of λ_j are found, which is the reason why no contribution of I and II for $\mu = 1.07$ in Fig. 4.14b is shown. This result is an artefact of the Monte-Carlo solver. In fact, directly at half-filling all eigenvalues and eigenvectors must be real, since $\chi^{\nu\nu'}$ is real and bisymmetric [11], however imaginary parts in the eigenvectors (but real eigenvalues) with an unusual oscillatory behaviour are also found at this temperature. This clearly indicates ergodicity problems in the CT-HYB Monte Carlo solver used for the calculations, for the bad-metallic/Mott insulating regime and low temperatures as $T = 1/120$.

(a)

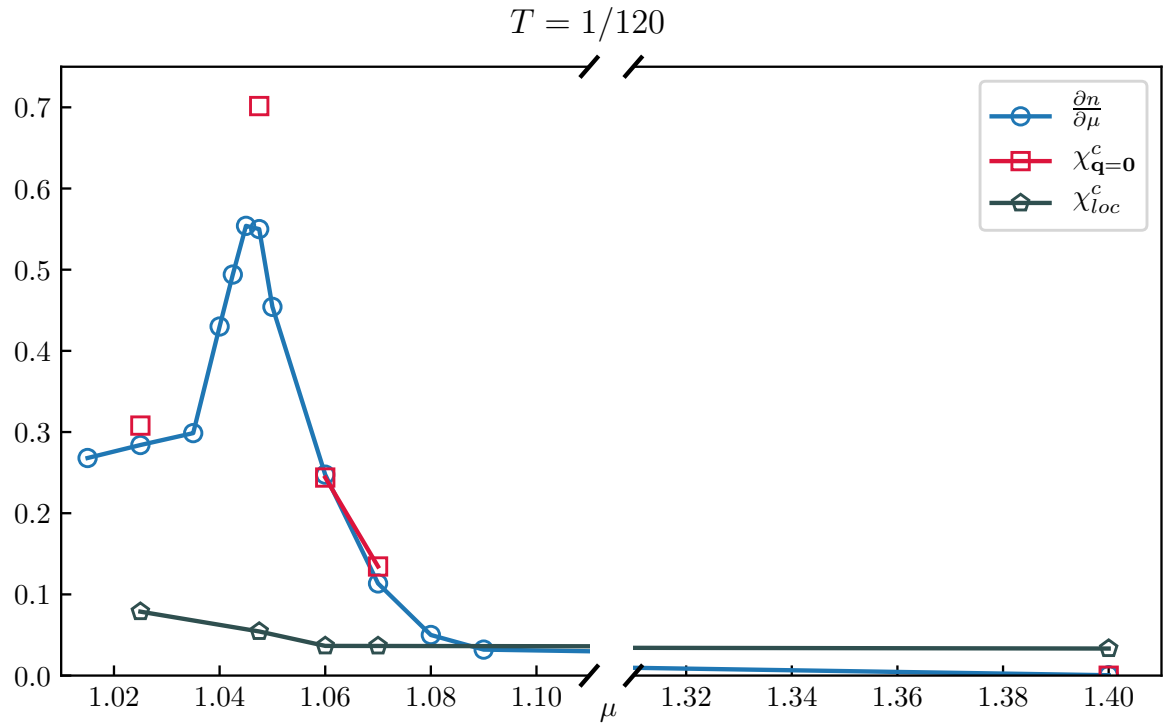

(b)

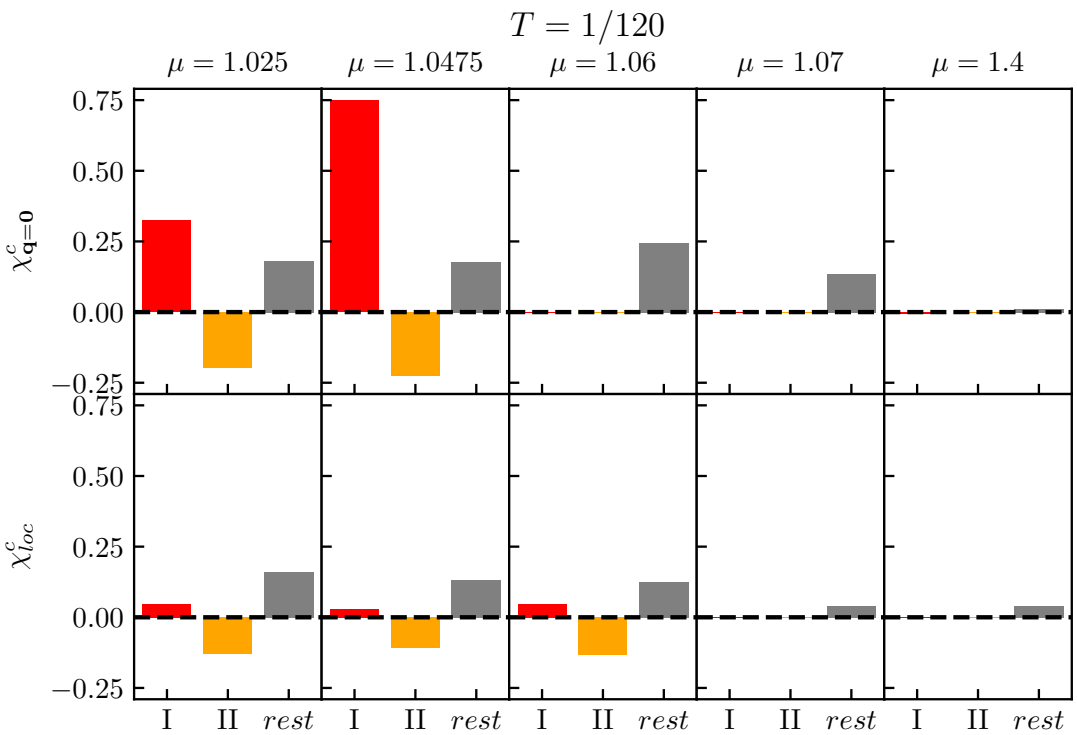

FIG. 4.14: (a): comparison of the numerical derivative $\partial n/\partial \mu$, the uniform charge susceptibility $\chi^c_{\mathbf{q}=\mathbf{0}}$, and the local charge susceptibility χ^c_{loc} for $T = 1/120$ and $U = 2.8$. (b): different contributions of $\chi^c = \mathrm{I} + \mathrm{II} + rest$ for different μ for the same T and U.

Chapter 5

Conclusion and Outlook

In this thesis we have clarified the direct relation between the divergences of the irreducible vertex functions and the enhancement of the compressibility κ in the close proximity to the critical endpoint of the Mott MIT in the single-band Hubbard model (on a square-lattice with $t = 1/4$, and out of half-filling)

For our analysis, we compared the physical *static* charge susceptibility $\chi^{c}_{\mathbf{q}=\mathbf{0}}$ – obtained from the two-particle generalised susceptibility $\chi^{\nu\nu'}_{c,\mathbf{q}=\mathbf{0}}$ – with the numerical derivative $\partial n/\partial\mu$. Thereby we performed DMFT calculations for two different parameter sets: ($U = 2.4,\ T = 1/50,\ 1/53$) very close to the critical endpoint of the MIT and ($U = 2.8,\ T = 1/120$) slightly more far away from half-filling ($n = 1$). The DMFT calculations for the one and two-particle quantities were performed with the *w2dynamics* package.

A great theoretical insight was achieved by considering the spectral decomposition of the generalised local charge susceptibility $\sum_{\nu\nu'} \chi^{\nu\nu'}_{c,loc} = \sum_j \lambda_j\, w_j$. The major role was played by two *real* and most negative eigenvalues, which can be unambiguously associated at lower U values with the first two divergences of the irreducible vertex Γ. Thereby, the lower of the two, λ_{I} – corresponding to an antisymmetric eigenvector with zero weight at $n = 1$ – yields an overall *positive* contribution $\lambda_{\mathrm{I}}\, w_{\mathrm{I}} > 0$ to the local physical charge susceptibility $\chi^{c}_{loc} = \frac{2}{\beta^2} \sum_j \lambda_j\, w_j$. This is possible, because $w_{\mathrm{I}} < 0$ at $n < 1$ due to the violation of the particle-hole symmetry upon doping. The second λ_{II}, however – associated to a symmetric eigenvector with positive weight at half-filling – still yields a negative contribution $\lambda_{\mathrm{II}}\, w_{\mathrm{II}} < 0$. By applying this spectral decomposition to the Bethe-Salpeter equation in DMFT:

$$\chi^{c}_{\mathbf{q}=\mathbf{0}} = \frac{2}{\beta^2} \sum_j (1/\lambda_j + t^2_{eff}/\beta)^{-1} w_j \tag{5.1}$$

we discovered, that indeed $\lambda_{\mathrm{I}} \to -t^2_{eff}/\beta$ drives the enhancement and eventually the divergence of $\chi^{c}_{\mathbf{q}=\mathbf{0}} \propto \kappa$ close to the MIT at $n < 1$. Since a negative λ_{I} is crucial for this mechanism, this can only occur after a divergence of the irreducible vertex Γ. This way, we have unveiled the exact mechanism controlling the enhancement of the uniform charge response in the non-perturbative regime, which can be interpreted, to a certain extent, as an effective attraction emerging from a strong local repulsion. At the same time, this means that approximation schemes where the irreducible vertex does not diverge (such as RPA, FLEX, fRG, the parquet approximation, etc.) cannot – per construction – capture this behaviour.

By extending this spectral analysis to the $\mathbf{q}$-dependence of the charge susceptibility, we showed that for the single-band Hubbard model in DMFT, the attractive effect is confined in an narrow region very close to $\mathbf{q} = \mathbf{0}$.

It is insightful to consider, eventually, also the spin and pairing (particle particle)

susceptibilities. The corresponding DMFT expression for the pairing susceptibility at $\mathbf{q} = \mathbf{0}$ (and also for the charge and spin susceptibility at $\mathbf{q} = \pi$) reads $\chi^{pp}_{\mathbf{q}=\mathbf{0}} = \frac{2}{\beta^2} \sum_j (1/\lambda_j - t^2_{eff}/\beta)^{-1} w_j$ [46]. This shows that possible divergences here are triggered by large positive eigenvalues. Therefore, the same effective attraction driven by negative eigenvalues of the local susceptibilities cannot result in charge density waves or s-wave pairing. However, the situation may be different in the case of multiorbital systems, strongly motivating further research in this direction.

Another open question, requiring further investigation, is how this attractive effect, driven by $\lambda_{\mathrm{I}}\, w_{\mathrm{I}} > 0$, gets encoded in the full vertex F, as this quantity can be directly connected to the Fermi liquid parameters.

Chapter 6

Appendix

6.1 Derivation of the Compressibility

The electronic compressibility is defined as the relative volume change against pressure for a fixed number of particles N and fixed temperature T:

$$\kappa = -\frac{1}{V}\left.\frac{\partial V}{\partial P}\right|_{T,N}. \tag{6.1}$$

It can be expressed depending on chemical potential μ and density $n = N/V$ by

$$\kappa = \frac{1}{n^2}\left.\frac{\partial n}{\partial \mu}\right|_{T}. \tag{6.2}$$

Following Ref. [47] we prove Eq. (6.2). Since P and μ are intensive variables of the system, scaling the system size by a factor a will leave them unchanged, whereas extensive variables like V and N will be scaled with a:

$$P(T,V,N) = P(T,aV,aN) \quad \text{and} \quad \mu(T,V,N) = \mu(T,aV,aN). \tag{6.3}$$

Taking the derivative with respect to a and evaluating at $a = 1$ will give

$$V\left.\frac{\partial P}{\partial V}\right|_{T,N} + N\left.\frac{\partial P}{\partial N}\right|_{T,V} = 0 \quad \text{and} \quad V\left.\frac{\partial \mu}{\partial V}\right|_{T,N} + N\left.\frac{\partial \mu}{\partial N}\right|_{T,V} = 0. \tag{6.4}$$

From the total derivative of the Helmholtz free energy

$$\mathrm{d}F = -S\mathrm{d}T - P\mathrm{d}V + \mu\mathrm{d}N \tag{6.5}$$

we find

$$-\left.\frac{\partial P}{\partial N}\right|_{T,V} = \frac{\partial^2 F}{\partial N \partial V} = \frac{\partial^2 F}{\partial V \partial N} = \left.\frac{\partial \mu}{\partial V}\right|_{T,N} \tag{6.6}$$

which leads together with Eq. (6.4) to

$$\frac{1}{\kappa} = -V\left.\frac{\partial P}{\partial V}\right|_{T,N} = N\left.\frac{\partial P}{\partial N}\right|_{T,V} = -N\left.\frac{\partial \mu}{\partial V}\right|_{T,N} = n^2\left.\frac{\partial \mu}{\partial n}\right|_{T}. \tag{6.7}$$

□

6.2 Static Physical Charge Susceptibility

For the density fluctuations in a grand canonical ensemble we recall the relation

$$\langle \hat{\mathcal{N}}^2 \rangle - \langle \hat{\mathcal{N}} \rangle^2 = \frac{1}{\beta^2} \frac{1}{Z} \frac{\partial^2 Z}{\partial \mu^2} - \left(\frac{1}{\beta} \frac{1}{Z} \frac{\partial Z}{\partial \mu} \right)^2 = \frac{1}{\beta} \frac{\partial}{\partial \mu} \left(\frac{1}{\beta} \frac{1}{Z} \frac{\partial Z}{\partial \mu} \right) = \frac{1}{\beta} \frac{\partial \langle \hat{\mathcal{N}} \rangle}{\partial \mu}, \tag{6.8}$$

where Z is the partition sum

$$Z = \mathrm{Tr} \left(\mathrm{e}^{-\beta(\hat{\mathcal{H}} - \mu \hat{\mathcal{N}})} \right). \tag{6.9}$$

This coincides with the physical charge susceptibility for $\mathbf{q} = \mathbf{0}$, since

$$\chi^c_{\mathbf{q}=\mathbf{0}}(\omega) = \int_0^\beta \mathrm{d}\tau \ \mathrm{e}^{\mathrm{i}\omega\tau} \langle \hat{n}(\tau) \hat{n}(0) \rangle - \beta \delta_{\omega 0} \langle \hat{n} \rangle^2 , \tag{6.10}$$

where $\hat{n} = \sum_{\sigma, \mathbf{k}} \hat{c}^\dagger_{\mathbf{k},\sigma} \hat{c}_{\mathbf{k}+\mathbf{0},\sigma}$. By evaluating the expectation value in the Eigenbasis $|m\rangle$ of $\hat{\mathcal{H}}$ and inserting a complete set of states $\sum_l |l\rangle \langle l|$ we find

$$\begin{aligned} \langle \hat{n}(\tau) \hat{n}(0) \rangle &= \frac{1}{Z} \sum_{m,l} \mathrm{e}^{-\beta \epsilon_m} \ \mathrm{e}^{\epsilon_m \tau} \langle m | \hat{n} | l \rangle \, \mathrm{e}^{-\epsilon_l \tau} \langle l | \hat{n} | m \rangle \\ &= \frac{1}{Z} \sum_m \mathrm{e}^{-\beta \epsilon_m} \langle m | \hat{n} | m \rangle^2 = \left\langle \hat{n}^2 \right\rangle , \end{aligned} \tag{6.11}$$

since $\langle m | \hat{n} | l \rangle = \delta_{ml} \langle m | \hat{n} | m \rangle$. Thus, for $\omega = 0$ we get

$$\chi^c_{\mathbf{q}=\mathbf{0}}(0) = \beta \big(\langle \hat{n}^2 \rangle - \langle \hat{n} \rangle^2 \big) = \frac{\partial \langle \hat{n} \rangle}{\partial \mu} = \frac{\partial n}{\partial \mu}. \tag{6.12}$$

6.3 Numerical Derivative

The numerical derivative used for the calculation of $\partial n / \partial \mu$ stems from the Taylor expansion around some calculated data point $n(\mu_0)$ and neighbours at $n(\mu_0 + \Delta_\mu)$ and $n(\mu_0 - \widetilde{\Delta}_\mu)$:

$$\begin{aligned} \mathrm{I}: \quad & n(\mu_0 + \Delta_\mu) = n(\mu_0) + \Delta_\mu \ n'(\mu_0) + \Delta_\mu^2 \ n''(\mu_0) + ... \\ \mathrm{II}: \quad & n(\mu_0 - \widetilde{\Delta}_\mu) = n(\mu_0) - \widetilde{\Delta}_\mu \ n'(\mu_0) + \widetilde{\Delta}_\mu^2 \ n''(\mu_0) + ... \end{aligned}$$

Gaussian elimination of the terms of second order in Eq. I and II by discarding any higher order terms in the calculation leads to

$$\begin{aligned} \left. \frac{\partial n}{\partial \mu} \right|_{\mu_0} &= n'(\mu_0) \\ &\approx \frac{\widetilde{\Delta}_\mu}{\Delta_\mu + \widetilde{\Delta}_\mu} \frac{n(\mu_0 + \Delta_\mu) - n(\mu_0)}{\Delta_\mu} + \frac{\Delta_\mu}{\Delta_\mu + \widetilde{\Delta}_\mu} \frac{n(\mu_0) - n(\mu_0 - \widetilde{\Delta}_\mu)}{\widetilde{\Delta}_\mu}, \end{aligned} \tag{6.13}$$

which becomes the better known central derivative for $\Delta_\mu = \widetilde{\Delta}_\mu$:

$$n'(\mu_0) \approx \frac{1}{2} \frac{n(\mu_0 + \Delta_\mu) - n(\mu_0 - \Delta_\mu)}{\Delta_\mu}. \tag{6.14}$$

For the delimiting data points a simple difference quotient $\Delta n / \Delta \mu$ has been used.

6.4 Centrohermitian Matrices

Here we recall the properties of centrohermitian matrices following Ref. [45]. In this thesis we consider a centrohermitian matrix $M \in \mathbb{C}^{2n\times 2n}$, where n is the number of positive/negative Matsubara frequencies. M is called centrohermitian if it fulfils the following condition:

$$JMJ = \overline{M} \tag{6.15}$$

where J[1] is the counter identity matrix ($J^2 = \mathbb{1}$), given by

$$J = \begin{pmatrix} 0 & \dots & 0 & 1 \\ \vdots & \ddots & 1 & 0 \\ 0 & 1 & \ddots & \vdots \\ 1 & 0 & \dots & 0 \end{pmatrix} = \begin{pmatrix} \mathbb{0} & J \\ J & \mathbb{0} \end{pmatrix}. \tag{6.16}$$

Thus, we can write M in the following partitioned form:

$$M = \begin{pmatrix} A & J\overline{B}J \\ B & J\overline{A}J \end{pmatrix}, \tag{6.17}$$

where $A, B \in \mathbb{C}^{n\times n}$. Eigenvalues λ of M are either real or appear in complex conjugate pairs [45]:

$$\lambda \begin{cases} \in \mathbb{R} \\ \in \mathbb{C},\ \exists\bar{\lambda} \end{cases} . \tag{6.18}$$

If M fulfils the stricter condition:

$$JMJ = M \tag{6.19}$$

M is called centrosymmetric. Then, the corresponding eigenvectors of λ are either symmetric $J\mathbf{v} = \mathbf{v}$ or anti-symmetric $J\mathbf{v} = -\mathbf{v}$. If M also satisfies $M = M^T$ the matrix is bisymmetric [48].

6.5 Asymptotic of the generalised Susceptibility

The *w2dynamics* calculations of the generalised susceptibilities $\chi^{\nu\nu'}_{c,loc}$, $\chi^{\nu\nu'}_{c,\mathbf{q}}$ resolve only a finite $2n\times 2n$ matrix in Matsubara space, where n is again the number of positive/negative Matsubara frequencies ($\nu(n) = \pi/\beta(2n+1)$). To account for the missing high frequency dependence of $\chi^{\nu\nu'}_{c,\mathbf{q}}$ in the calculation of the physical susceptibility $\chi^{c}_{\mathbf{q}} = \frac{2}{\beta^2}\sum_{\nu\nu'}\chi^{\nu\nu'}_{c,\mathbf{q}}$ we use the fact that the higher Matsubara frequency dependence of $\chi^{\nu\nu'}_{c,loc}$, $\chi^{\nu\nu'}_{c,\mathbf{q}}$ is dominated by the asymptotic of the *bubble* contribution $\chi^{\nu\nu'}_{0}$: $\frac{\beta}{\nu^2}\delta_{\nu\nu'}$. Therefore we can extrapolate the high frequency asymptotic in two ways: (i) by gradually increasing the matrix size $2n\times 2n$ and summing over more and more Matsubara frequencies, we can fit the resulting curve via the least-square-error method to an approximative function $a + b/n$ with the correct asymptotic behaviour. For $n \to \infty$ we obtain the physical susceptibility as $\chi^{c}_{\mathbf{q}} \simeq a$. Or (ii) by calculating the contribution of the asymptotic summation of the bubble explicitly by $\chi^{c}_{\mathbf{q}} \simeq \frac{2}{\beta^2}\left(\sum_{\nu\nu'}^{\pm n}\chi^{\nu\nu'}_{c,\mathbf{q}} + 2\sum_{n}^{\infty}\delta_{\nu\nu'}\frac{\beta}{\nu^2}\right)$, where $\frac{4}{\beta^2}\sum_{n}^{\infty}\delta_{\nu\nu'}\frac{\beta}{\nu^2} = \frac{4\beta}{\pi^2}\left(\frac{\pi^2}{8} - \sum_{\tilde{n}=0}^{n}\frac{1}{(2\tilde{n}+1)^2}\right)$.

[1] Note that $M \to MJ$ corresponds to flipping every row in $M = (M_{ij})$ – $(M_{i1}M_{i2}\dots M_{i2n}) \to (M_{i2n}\dots M_{i2}M_{i1})$ – and $M \to JM$ flips every column, thus $M \to JMJ$ corresponds to a flip of each entry of M around the center.

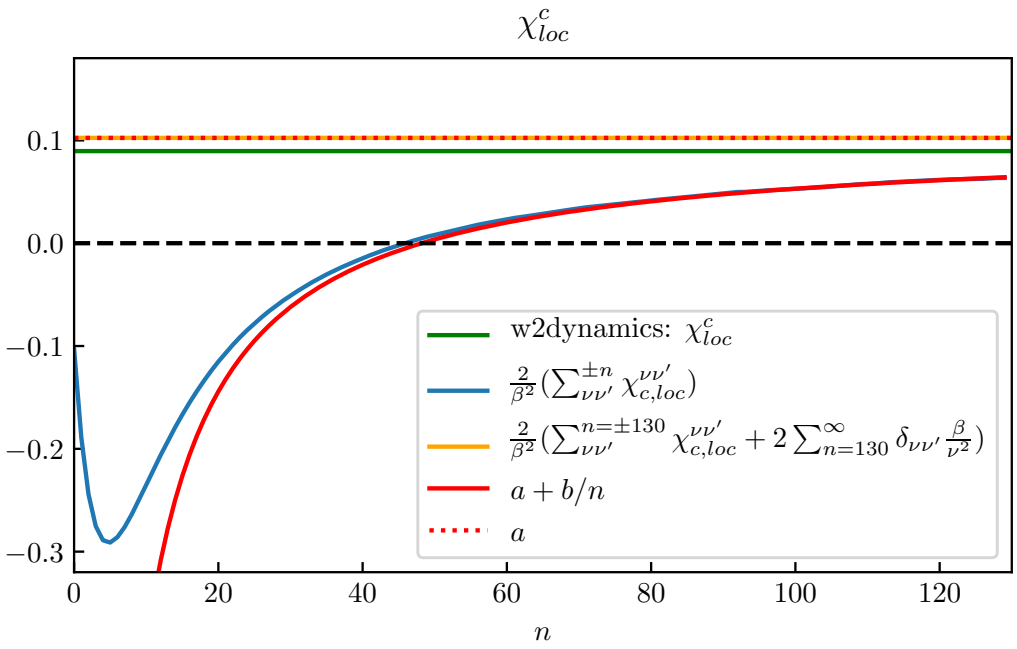

FIG. 6.1: Here we compare the different methods for accounting the high frequency dependence of $\chi^{\nu\nu'}_{c,loc}$ in the calculation of χ^c_{loc}. The green line represents the direct calculation in *w2dynamics*, the blue curve shows the summation over finite $2n \times 2n$ Matsubara space, where n is the number of positive/negative Matsubara frequencies. The orange line accounts for the asymptotic in the calculation of χ^c_{loc} by approximating $\chi^{\nu\nu'}_{c,loc}$ with $\frac{\beta}{\nu^2}\delta_{\nu\nu'}$ for $n > 130$ and the red line shows the least-square-error fitted function $a + b/n$ onto the asymptotic of the blue curve. Hence, a is an approximative value for χ^c_{loc}.

Since the local physical susceptibility $\chi^c_{loc} = \frac{2}{\beta^2}\sum_{\nu\nu'} \chi^{\nu\nu'}_{c,loc}$ can be directly calculated in *w2dynamics* it makes sense to compare here the two methods (Fig. 6.1): both methods yield identical results for the considered parameters ($U = 2.4,\ \beta = 50,\ \mu = 1.025$) and have a relative error in comparison with the directly calculated χ^c_{loc} of the order of $\approx 10\%$. For the calculation of $\chi^c_{\mathbf{q}}$ we favoured method (ii).

Bibliography

[1] P. Hohenberg and W. Kohn, Phys. Rev. **136**, B864 (1964).

[2] R. M. Martin, L. Reining, and D. M. Ceperley, *Interacting Electrons: Theory and Computational Approaches* (Cambridge University Press, 2016).

[3] W. Metzner and D. Vollhardt, Phys. Rev. Lett. **62**, 324 (1989).

[4] A. Georges, G. Kotliar, W. Krauth, and M. J. Rozenberg, Rev. Mod. Phys. **68**, 13 (1996).

[5] A. Toschi, A. A. Katanin, and K. Held, Phys. Rev. B **75**, 045118 (2007).

[6] G. Rohringer, H. Hafermann, A. Toschi, A. A. Katanin, A. E. Antipov, M. I. Katsnelson, A. I. Lichtenstein, A. N. Rubtsov, and K. Held, Rev. Mod. Phys. **90**, 025003 (2018).

[7] T. Schäfer, G. Rohringer, O. Gunnarsson, S. Ciuchi, G. Sangiovanni, and A. Toschi, Phys. Rev. Lett. **110**, 246405 (2013).

[8] T. Schäfer, S. Ciuchi, M. Wallerberger, P. Thunström, O. Gunnarsson, G. Sangiovanni, G. Rohringer, and A. Toschi, Phys. Rev. B **94**, 235108 (2016).

[9] J. Vučičević, N. Wentzell, M. Ferrero, and O. Parcollet, Phys. Rev. B **97**, 125141 (2018).

[10] P. Chalupa, P. Gunacker, T. Schäfer, K. Held, and A. Toschi, Phys. Rev. B **97**, 245136 (2018).

[11] D. Springer, P. Chalupa, S. Ciuchi, G. Sangiovanni, and A. Toschi, Interplay between local response and vertex divergences in many-fermion systems with on-site attraction (2019), arXiv:1912.02546 [cond-mat.str-el] .

[12] E. Kozik, M. Ferrero, and A. Georges, Phys. Rev. Lett. **114**, 156402 (2015).

[13] O. Gunnarsson, G. Rohringer, T. Schäfer, G. Sangiovanni, and A. Toschi, Phys. Rev. Lett. **119**, 056402 (2017).

[14] G. Kotliar, S. Murthy, and M. J. Rozenberg, Phys. Rev. Lett. **89**, 046401 (2002).

[15] R. Nourafkan, M. Côté, and A.-M. S. Tremblay, Phys. Rev. B **99**, 035161 (2019).

[16] G. D. Mahan, *Many-particle physics* (Springer Science & Business Media, 2013).

[17] A. A. Abrikosov, L. P. Gorkov, and I. E. Dzyaloshinski, *Methods of quantum field theory in statistical physics* (Courier Corporation, 2012).

[18] W. Nolting, *Grundkurs Theoretische Physik* (Springer, 2005).

[19] G. Rohringer, *New routes toward a theoretical treatment of nonlocal electronic correlations*, Ph.D. thesis, Technischen Universität Wien (2014).

[20] G. Rohringer, A. Valli, and A. Toschi, Phys. Rev. B **86**, 125114 (2012).

[21] N. Bickers, in *Theoretical Methods for Strongly Correlated Electrons* (Springer, 2004) pp. 237–296.

[22] M. Reitner, *Generalized Susceptibilities of the Anderson Impurity Model: Fingerprints of Local Moment Physics and Kondo Screening at the Two-Particle Level*, Project work, Technischen Universität Wien (2019).

[23] F. Krien, E. G. C. P. van Loon, M. I. Katsnelson, A. I. Lichtenstein, and M. Capone, Phys. Rev. B **99**, 245128 (2019).

[24] E. Koch, E. Pavarini, and S. Zhang, *Many-Body Methods for Real Materials*, Vol. 9 (Forschungszentrum Jülich, 2019).

[25] G. Kotliar, The European Physical Journal B-Condensed Matter and Complex Systems **11**, 27 (1999).

[26] M. Wallerberger, A. Hausoel, P. Gunacker, A. Kowalski, N. Parragh, F. Goth, K. Held, and G. Sangiovanni, Computer Physics Communications **235**, 388 (2019).

[27] E. Gull, A. J. Millis, A. I. Lichtenstein, A. N. Rubtsov, M. Troyer, and P. Werner, Rev. Mod. Phys. **83**, 349 (2011).

[28] M. Reitner, P. Chalupa, L. D. Re, D. Springer, S. Ciuchi, G. Sangiovanni, and A. Toschi, Attractive effect of a strong electronic repulsion – the physics of vertex divergences (2020), arXiv:2002.12869 [cond-mat.str-el] .

[29] C. Walsh, P. Sémon, D. Poulin, G. Sordi, and A.-M. S. Tremblay, Phys. Rev. B **99**, 075122 (2019).

[30] N. Goldenfeld, *Lectures on phase transitions and the renormalization group* (CRC Press, 2018).

[31] T. Moriya, *Spin fluctuations in itinerant electron magnetism*, Vol. 56 (Springer Science & Business Media, 2012).

[32] K. Haule and G. Kotliar, New Journal of Physics **11**, 025021 (2009).

[33] L. de' Medici, J. Mravlje, and A. Georges, Phys. Rev. Lett. **107**, 256401 (2011).

[34] E. Pavarini, E. Koch, A. Lichtenstein, and D. Vollhardt, *The LDA+DMFT approach to strongly correlated materials*, Vol. 1 (Forschungszentrum Jülich, 2011).

[35] T. Ribic, E. Assmann, A. Tóth, and K. Held, Phys. Rev. B **90**, 165105 (2014).

[36] M. Berovic, *Exploring Hund's correlated metals: charge instabilities and effect of selective interactions*, Ph.D. thesis, International School for Advanced Studies (2018).

[37] A. Isidori, M. Berović, L. Fanfarillo, L. de' Medici, M. Fabrizio, and M. Capone, Phys. Rev. Lett. **122**, 186401 (2019).

[38] L. de' Medici, Phys. Rev. Lett. **118**, 167003 (2017).

[39] M. C. et al., (2020), unpublished.

[40] L. D. Re and A. Toschi, The dynamical vertex approximation of systems with broken SU(2)-symmetry (2020), unpublished.

[41] A. A. Katanin, A. Toschi, and K. Held, Phys. Rev. B **80**, 075104 (2009).

[42] G. Rohringer and A. Toschi, Phys. Rev. B **94**, 125144 (2016).

[43] E. G. C. P. van Loon, H. Hafermann, A. I. Lichtenstein, and M. I. Katsnelson, Phys. Rev. B **92**, 085106 (2015).

[44] K. Van Houcke, F. Werner, T. Ohgoe, N. V. Prokof'ev, and B. V. Svistunov, Phys. Rev. B **99**, 035140 (2019).

[45] A. Lee, Linear Algebra and its Applications **29**, 205 (1980), special Volume Dedicated to Alson S. Householder.

[46] L. D. Re and G. Rohringer, (2020), unpublished.

[47] F. Schwabel, *Statistische Mechanik* (Springer-Verlag Berlin Heidelberg New York, 2000).

[48] R. M. Reid, SIAM Review **39**, 313 (1997).